

# Neural Optical Flow for Planar and Stereo PIV

Andrew I. Masker\*, Ke Zhou\*, Joseph P. Molnar, and Samuel J. Grauer†

Department of Mechanical Engineering, Pennsylvania State University

## Abstract

Neural optical flow (NOF) offers improved accuracy and robustness over existing OF methods for particle image velocimetry (PIV). Unlike other OF techniques, which rely on discrete displacement fields, NOF parameterizes the physical velocity field using a continuous neural-implicit representation. This formulation enables efficient data assimilation and ensures consistent regularization across views for stereo PIV. The neural-implicit architecture provides significant data compression and supports a space–time formulation, facilitating the analysis of both steady and unsteady flows. NOF incorporates a differentiable, nonlinear image-warping operator that relates particle motion to intensity changes between frames. Discrepancies between the advected intensity field and observed images form the data loss, while soft constraints, such as Navier–Stokes residuals, enhance accuracy and enable direct pressure inference from PIV images. Additionally, mass continuity can be imposed as a hard constraint for both 2D and 3D flows. Implicit regularization is achieved by tailoring the network’s expressivity to match a target flow’s spectral characteristics. Results from synthetic planar and stereo PIV datasets, as well as experimental planar data, demonstrate NOF’s effectiveness compared to state-of-the-art wavelet-based OF and CC methods. Additionally, we highlight its potential broader applicability to techniques like background-oriented schlieren, molecular tagging velocimetry, and other advanced measurement systems.

**Keywords:** particle image velocimetry, stereoscopic PIV, optical flow, scientific machine learning, inverse problems

## 1 Introduction

Enhanced processing techniques for particle image velocimetry (PIV) have significantly improved the accuracy and resolution of velocity measurements [1]. PIV is a widely used, non-intrusive technique that captures 2D–3D velocity fields from images of a particle-laden flow exposed to a pulsed laser sheet or slab [2]. Tracer particles are advected between frames, illuminated by the laser, and imaged; sequential images are processed using a computer vision algorithm, cross-correlation (CC) algorithm, or similar to determine the particle displacement field. This field is converted to a velocity field, assuming a constant velocity between frames. Spatially resolved velocity fields obtained through PIV can reveal key flow features such as vortices, separation bubbles, and organized packets of coherent structures [3]. Furthermore, velocity may be used to calculate other fields like pressure, vorticity, strain rate, and Reynolds stresses, which are essential for characterizing the performance of engineering devices and validating computational models [4, 5]. Despite the success of current methods, however, the need for more accurate measurements and greater resolution continues to drive the development of improved PIV techniques.

Cross-correlation is the standard method for extracting velocity fields from pairs of particle images in PIV. In this approach, images are divided into smaller regions called interrogation windows, and the correlation between windows in successive frames is computed to determine the average displacement of particles inside the window. The most probable displacement is identified by the peak correlation between windows across the image pair [1]. A single velocity vector is generated for each interrogation window, and these windows are typically overlapped by 50–75% to produce a denser vector field. Multi-resolution techniques are also employed to improve the performance of CC by estimating a coarse displacement field using large windows, warping one of the images accordingly, estimating a finer displacement field with

---

\* Authors made an equal contribution.

† Corresponding author: [sgrauer@psu.edu](mailto:sgrauer@psu.edu)

smaller windows, and iterating this process. Hu et al. [6] found that optimal results are achieved when the smallest interrogation window is large enough to contain multiple particles but small enough to minimize excessive smoothing, typically ranging in size from  $16 \times 16$  to  $32 \times 32$  pixels. Nevertheless, even under optimal conditions, CC displacement yields fields with a vector spacing of about five pixels, causing velocity and gradient fields to appear smeared or low-pass filtered [6–8]. Although significant efforts have been made to improve the resolution of CC-based measurements [7, 9–13], modern implementations still produce a relatively coarse deflection field. Despite these drawbacks, CC remains the most widely used technique for PIV analysis due to its computational speed, simplicity, and reliable performance.

Optical flow (OF) offers an alternative approach to PIV by computing a displacement field that warps an image taken at time  $t$  to match the image from time  $t + \Delta t$ . OF algorithms can generate a dense velocity field, with one vector per pixel,<sup>1</sup> making them particularly effective for capturing flows with broadband spectral content and sharp gradients. However, classical OF methods are limited to handling small displacements [14], usually requiring a multi-resolution scheme to accommodate larger displacements [15, 16]. These schemes can struggle with flows featuring both high gradients and a wide range of scales, such as turbulent shear layers or boundary layers [17]. Hybrid approaches that integrate OF with CC have been proposed to address these issues, but they introduce additional parameters to tune and increase computational complexity [15, 18]. Since OF is inherently ill-posed, regularization is required to obtain a stable solution; in most cases, the regularization parameters are heuristically tuned for each flow scenario [19]. Despite its advantages in accuracy and resolution, the adoption of OF for PIV has been limited due to its higher computational cost compared with CC, and its sensitivity to spatiotemporal variations in laser output and out-of-plane motion, both of which amplify errors.

Wavelet-based optical flow (WOF) is the state of the art in OF for PIV. Introduced by Wu et al. [20] and further developed by Dérian et al. [21], WOF represents the displacement field in the wavelet domain, taking advantage of the inherent multi-scale nature of the wavelet transform [22] to resolve turbulent flows with significant scale separation. Displacement estimates are refined using a coarse-to-fine approach, progressively optimizing wavelet coefficients across successive levels of the transform. Regularization is applied either by truncating the transform or adding a penalty term that promotes smoothness and stability. The wavelet coefficients are optimized via gradient descent, with spatial gradients in the penalty term computed directly in the wavelet domain [21, 23]. Schmidt and Sutton [8, 24] benchmarked WOF against state-of-the-art CC methods across various flow scenarios and particles-per-pixel (ppp) values, demonstrating that WOF consistently outperforms CC, especially at high wavenumbers and in capturing gradients, leading to more accurate vorticity fields. More recently, Jassal and Schmidt [25] and Nicolas et al. [26] highlighted WOF's advantages in recovering near-wall velocity content.

The rapid adoption of machine learning (ML) in fluid dynamics has been driven by its success in other fields and the suitability of ML methods for image processing. These strengths make ML a natural fit for analyzing data from fluid diagnostics. One of the earliest breakthroughs in ML for fluid applications involved convolutional neural networks (CNNs), which excel at processing image data embedded in a low-dimensional, nonlinear manifold [27–31]. Building on this foundation, CNNs have been applied to PIV processing. Rabault et al. [32] and Lee et al. [33] developed CNN models for end-to-end motion estimation from particle images, mimicking CC in producing a sparse velocity field with one vector per image window, e.g.,  $32 \times 32$  pixels in size. Cai et al. [34, 35] augmented this approach to achieve dense motion estimation, generating one vector per pixel with accuracy comparable to Horn–Schunck OF [35]. However, CNN-based algorithms require extensive pre-training on large, labeled datasets, typically comprising synthetic PIV images produced via direct numerical simulations (DNSs). This dependence on specific training data introduces the risk of overfitting and limits the generalizability of the trained models to unseen flow scenarios.

Neural-implicit fields are an emerging paradigm in computer vision and scientific ML that operate in an unsupervised manner [36–39]. These networks, termed coordinate neural networks, represent variables as a continuous function of the input coordinates through one or more neural networks, providing significant data compression, particularly for spatio-temporally resolved fields [37]. Exact partial derivatives of the networks can be efficiently computed via automatic differentiation, making these representations ideal for gradient-based optimization and data assimilation [40, 41], where the inferred fields are known

---

<sup>1</sup>Although the number and arrangement of displacement vectors can vary, it is standard to estimate one vector per pixel.

to satisfy differential equations. Unlike CNNs and other supervised models, coordinate neural networks can circumvent the need for labeled datasets, overcoming a key limitation of most ML methods used for PIV processing. Their versatility has led to applications in neural radiance fields for novel view synthesis [38, 39], tomographic imaging [42–44], and data assimilation [45–47]

Recently, Qi et al. [48] introduced a neural-implicit OF algorithm for PIV, demonstrating its ability to handle large displacements and enforce physical constraints through a Helmholtz decomposition. However, their method relies on “HDNet,” a differentiable Poisson solver trained on extensive synthetic datasets. This component reintroduces challenges typical of supervised learning and may limit generalizability, as seen in CNN-based PIV methods.

We present *neural optical flow* (NOF), a framework that builds on the neural-implicit approach to modeling flow fields. NOF also incorporates a differentiable, nonlinear image-warping operator to estimate large displacements without the need for a multi-resolution scheme. The velocity field in world space is represented as a continuous function of space and time, making the method naturally extensible to higher-dimensional techniques like stereo or tomographic PIV. This space–time formulation offers substantial compression, reduces computational costs, and ensures seamless handling of steady and unsteady flows.

Our framework leverages the strengths of Qi et al.’s neural-implicit OF method while eliminating the need for HDNet to enforce mass continuity. We achieve this by embedding continuity as a hard constraint through scalar or vector velocity potential fields and incorporating the Navier–Stokes equations into the optimization process, transforming NOF into a physics-informed neural network (PINN) [40]. By incorporating governing equations, our method operates as a PINN-based data assimilation algorithm, providing continuous, analytical representations of flow variables (e.g., velocity, pressure) that are trained to obey physical laws. Regularization is achieved by minimizing equation residuals, facilitating accurate flow reconstruction from sparse measurements and enabling direct pressure inference from PIV images [49].

In addition to supporting data assimilation, NOF natively integrates stereo PIV by employing forward and inverse camera transforms to map between sensor and world coordinates. This allows us to use a single, continuous velocity field across both perspectives, ensuring consistent regularization. NOF improves upon previous PINN-based methods, such as that of Cai et al. [49], by moving beyond the linear OF equation, making our approach more effective for turbulent flows with a broad range of spectral content.

By combining the frameworks of Qi et al. [48] and Cai et al. [49], with our own innovations, we introduce a more accurate and robust OF technique. We validate NOF on both synthetic and experimental PIV datasets, comparing its performance to conventional CC and a state-of-the-art wavelet-based OF method. Our results demonstrate NOF’s superior accuracy, robustness, and computational efficiency across a range of scenarios. The remainder of this paper is organized as follows: Sec. 2 introduces the concepts underlying NOF. In Sec. 3, we describe the synthetic and experimental flow cases used for evaluation. Numerical and experimental results are then presented in Secs. 4 and 5, respectively, followed by our conclusions.

## 2 Methodology

Neural optical flow estimates the fluid motion that warps the first particle image in a pair to match the second image. To facilitate our discussion, we first introduce the coordinate transformations between the world and sensor spaces. Light captured by the cameras originates from the 2D plane of the laser sheet,  $\mathcal{P}$ , which comprises a set of 3D points in world space,  $\mathbf{x} = (x_1, x_2, x_3) \in \mathcal{P}$ . Images are resolved in the sensor space,  $\mathcal{S}$ , where  $\mathbf{s} = (s_1, s_2) \in \mathcal{S}$  represents a position on the sensor in pixel units. There is a unique mapping between  $\mathcal{P}$  and  $\mathcal{S}$  in both directions. The forward mapping, or “camera transform,” is defined as

$$\Psi : \mathcal{P} \rightarrow \mathcal{S}, \tag{1}$$

and the inverse mapping, or inverse camera transform, is

$$\Psi^{-1} : \mathcal{S} \rightarrow \mathcal{P}. \tag{2}$$

Examples of  $\Psi$  and  $\Psi^{-1}$  relevant to PIV are provided in [Appendix A](#). Two additional quantities are essential: (1) the magnification of the optical system for light from a point  $\mathbf{x}$ ,

$$M = \frac{f}{|\mathbf{x} - \mathbf{c}| - f} \quad , \tag{3}$$

where  $\mathbf{c}$  denotes the camera’s position and  $f$  is the focal length of the lens, and (2) the pixel pitch,  $\psi$ , defined as the reciprocal of the pixel size. With these elements in hand, we can describe the estimation of velocity fields from PIV data.

In the following sections, we introduce a differentiable image-warping operator and demonstrate its use in data losses for planar and stereo PIV. We then explore various regularization techniques, including both physics-*inspired* and physics-*informed* methods.

## 2.1 Neural Optical Flow

Optical flow is a computer vision method used to estimate the *apparent* motion in a sequence of images based on changes in intensity. Over the years, many variations of OF have been developed, leveraging pixel-based methods, wavelets, or neural networks, as reviewed by Mendes et al. [50]. Our NOF technique builds on these approaches by employing a neural-implicit representation of the physical velocity field. Like other OF algorithms, NOF assumes that the brightness of a displaced feature is conserved between consecutive frames:

$$I(\mathbf{s}, t) = I(\mathbf{s} + \Delta\mathbf{s}, t + \Delta t). \quad (4)$$

Here,  $I$  is the image intensity at a sensor position  $\mathbf{s}$  and time  $t$ ;  $\Delta\mathbf{s}$  and  $\Delta t$  are the image displacement and time interval between frames, respectively.

In PIV, the displacement of a visible feature (usually a bright spot) in the image corresponds to the advection of a particle by the fluid in world space,

$$\Delta\mathbf{x} = \int_t^{t+\Delta t} \underbrace{\frac{d\tilde{\mathbf{x}}(\tau)}{d\tau}}_{\mathbf{v}(\tilde{\mathbf{x}}, \tau)} d\tau, \quad (5a)$$

where  $\tilde{\mathbf{x}}$  is the streamline starting from position  $\mathbf{x}$  at time  $t$  and  $\mathbf{v} = (v_1, v_2, v_3)$  is the fluid velocity. The physical displacement is then projected onto the camera sensor,

$$\Delta\mathbf{s} \equiv \underbrace{\Psi(\mathbf{x} + \Delta\mathbf{x})}_{\mathbf{s} + \Delta\mathbf{s}} - \underbrace{\Psi(\mathbf{x})}_{\mathbf{s}}. \quad (5b)$$

OF aims to solve for the apparent displacement,  $\Delta\mathbf{s}$ , which evolves the image intensity  $I$  from time  $t$  to  $t + \Delta t$ . Once  $\Delta\mathbf{s}$  is determined, it is mapped back to the two in-plane displacement components,  $(\Delta x_1, \Delta x_2)$ .<sup>2</sup> The fluid velocity is then approximated as  $\mathbf{v} \approx \Delta\mathbf{x}/\Delta t$ .

Solving for  $\Delta\mathbf{s}$  using Eq. (4) is a challenging nonlinear optimization problem. A common simplification is to approximate the right-hand side with a first-order Taylor series expansion, evaluated at  $(\mathbf{s}, t)$ ,

$$I \approx I + \frac{dI}{dt} \Delta t \quad (6a)$$

$$= I + \left( \frac{\Delta\mathbf{s}}{\Delta t} \cdot \nabla_{\mathbf{s}} I + \frac{\partial I}{\partial t} \right) \Delta t, \quad (6b)$$

where  $\partial I/\partial t$  is approximated by  $[I(\mathbf{x}, t + \Delta t) - I(\mathbf{x}, t)]/\Delta t$  and  $\nabla_{\mathbf{s}}$  is the gradient operator in sensor coordinates. As  $\Delta t \rightarrow 0$ , we get the linear OF equation,

$$\frac{\partial I}{\partial t} + \mathbf{v}_S \cdot \nabla_{\mathbf{s}} I = 0, \quad (7)$$

where  $\mathbf{v}_S$  is the apparent velocity in the image, which can be scaled by  $(\psi M)^{-1}$  to estimate  $\mathbf{v}$ . While this linearization works well for small displacements, it breaks down as  $\Delta\mathbf{s}$  or  $\Delta t$  becomes large [15, 18, 51]. A robust motion estimation algorithm must effectively handle large displacements, so we adopt the generalized OF model from Eq. (4) for this work.

Motion estimation by OF is formulated as an optimization problem with a data loss term, expressed either in integral form,

$$\mathcal{J}_{\text{data}} = \frac{1}{|\mathcal{S}|} \int_{\mathcal{S}} [I(\mathbf{s}, t) - I(\mathbf{s} + \Delta\mathbf{s}, t + \Delta t)]^2 d\mathbf{s}, \quad (8a)$$

<sup>2</sup>This assumes the laser sheet aligns with the  $(x_1, x_2)$  coordinates, otherwise a coordinate transformation is required.

or differential form,

$$\mathcal{J}_{\text{data}} = \frac{1}{|\mathcal{S}|} \int_{\mathcal{S}} \left( \frac{\partial I}{\partial t} + \frac{\Delta \mathbf{s}}{\Delta t} \cdot \nabla_{\mathbf{s}} I \right)^2 d\mathbf{s}. \quad (8b)$$

The latter assumes the linearization in Eq. (6). Either way, the objective is to find the displacement  $\Delta \mathbf{s}$  that minimizes  $\mathcal{J}_{\text{data}}$ . This is an ill-posed inverse problem with no unique solution, having only one piece of information from each pixel (i.e., the intensity) and two unknown parameters,  $(\Delta s_1, \Delta s_2)$ : an issue known as the ‘‘aperture problem’’ [52]. To ensure a unique, physically plausible solution, most OF techniques introduce an explicit penalty term,  $\mathcal{J}_{\text{penalty}}$ , which promotes desirable characteristics, such as spatial smoothness, in the solution. The total loss function is a weighted sum of the data and penalty terms,

$$\mathcal{J}_{\text{total}} = \mathcal{J}_{\text{data}} + \lambda \mathcal{J}_{\text{penalty}} \quad (9)$$

The weighting parameter  $\lambda$  must be carefully selected to balance the losses. The optimal displacement field,  $\Delta \mathbf{s}^*$ , is obtained by minimizing the total loss,

$$\Delta \mathbf{s}^* = \arg \min_{\Delta \mathbf{s}} \mathcal{J}_{\text{total}}. \quad (10)$$

Neural optical flow is distinguished by its use of a neural-implicit representation of the velocity field. Rather than relying on pixel- or wavelet-based methods, a neural network,  $\mathcal{N}$ , models the fluid velocity as a continuous function of space and time,

$$\mathcal{N} : (\mathbf{x}, t) \mapsto \mathbf{v}. \quad (11)$$

In other words,  $\mathcal{N}$  is a network that takes  $\mathbf{x}$  and  $t$  as inputs and outputs  $\mathbf{v}$ . Additional variables like pressure can also be outputted, as demonstrated in Sec. 4.3. Details of the network architecture are provided in Appendix B. Given an estimated velocity field from  $\mathcal{N}$ , the following sequence is used to compute the displacement and objective loss:

1. **Compute physical displacement:** A displacement  $\Delta \mathbf{x}$  is obtained by numerically integrating the velocity field  $\mathbf{v}$  using Eq. (5a).
2. **Transform to sensor space:** The physical displacement is projected onto the sensor as  $\Delta \mathbf{s}$  via Eq. (5b).
3. **Evaluate intensities for data loss:** The intensities  $I(\mathbf{s}, t)$  and  $I(\mathbf{s} + \Delta \mathbf{s}, t + \Delta t)$  are sampled for use in the integral-form data loss, Eq. (8a).

The following section details and visually presents these steps.

The NOF framework offers several advantages over existing OF methods. First, numerical integration of the velocity field allows it to handle large displacements without requiring a multi-resolution scheme [19, 34, 35, 53, 54]. Second, NOF extends naturally to stereo PIV, as discussed in Sec. 2.3: the neural network represents all three velocity components in physical space and optimizes across both imaging perspectives simultaneously. Third, the method leverages a  $C^\infty$  neural representation, enabling continuous regularization through automatic differentiation, as outlined in Sec. 2.4. Implicit regularization is also achieved by tuning the spectral content embedded in the network’s Fourier encoding, per Appendix B. Lastly, both weak- and hard-form physics-based constraints are introduced to refine velocity estimates and infer additional flow states, such as pressure, which is described in Sec. 2.5.

## 2.2 Data Loss for Planar PIV

A key element of any OF technique is the warping operator, as the quality of the velocity field is assessed by warping the first image to approximate the second one. An ideal warping operator,  $\mathcal{W}$ , can be defined in terms of the sets

$$\mathcal{I}(t) = \{I(\mathbf{s}, t) \mid \mathbf{s} \in \mathcal{S}\} \quad \text{and} \quad \delta \mathcal{S} = \{\Delta \mathbf{s}(\mathbf{s}) \mid \mathbf{s} \in \mathcal{S}\}, \quad (12)$$

where  $\mathcal{I}$  represents the imaged intensity field at time  $t$  across the sensor domain  $\mathcal{S}$ , and  $\delta \mathcal{S}$  is the deflection field. The warping operator acts on this set as

$$\mathcal{W} : (\mathcal{I}, \delta \mathcal{S}) \mapsto \mathcal{I}', \quad (13)$$

where  $\mathcal{I}'$  is the image warped by the displacement field  $\delta \mathcal{S}$ .

The linear OF warping operator, commonly used in OF algorithms, employs Eq. (7) to describe changes to the initial image. Discrete derivatives of  $I$ , evaluated at the pixel centroids, are combined with the estimated flow state to generate the warped image. This warped image is then compared to the experimental data, forming the objective loss in Eq. (8b).

The nonlinear warping operators used in conjunction with Eq. (8a) do not rely on such approximations. Nonlinear warping can be categorized into two classes. The first, more general approach advects the intensity at each position  $\mathbf{s}$  to  $\mathbf{s} + \Delta\mathbf{s}$ , with the warped image  $\mathcal{I}'$  comprising the sum of deposited intensities at these new locations. However, this formulation is non-injective and not invertible, as illustrated by the scenario where two points in the first frame advect to the same location in the second frame.

Many optimization schemes call for an invertible mapping. This second class of warping assumes injectivity, ensuring that the operator satisfies

$$\mathcal{W}(\mathcal{I}, \delta\mathcal{S}) = \mathcal{I}' \quad \text{and} \quad \mathcal{I} = \mathcal{W}(\mathcal{I}', -\delta\mathcal{S}). \quad (14)$$

With the added assumption of surjectivity, every point  $\mathbf{s} \in \mathcal{S}$  in the first frame maps to a unique point in the second frame, allowing the integrals in Eq. (8a) to be approximated to arbitrary precision. In this work, we adopt this assumption, implying that all positions in  $\mathcal{S}$  are advected to distinct locations on the sensor in the second frame. Our method remains robust even when these assumptions are not strictly met.

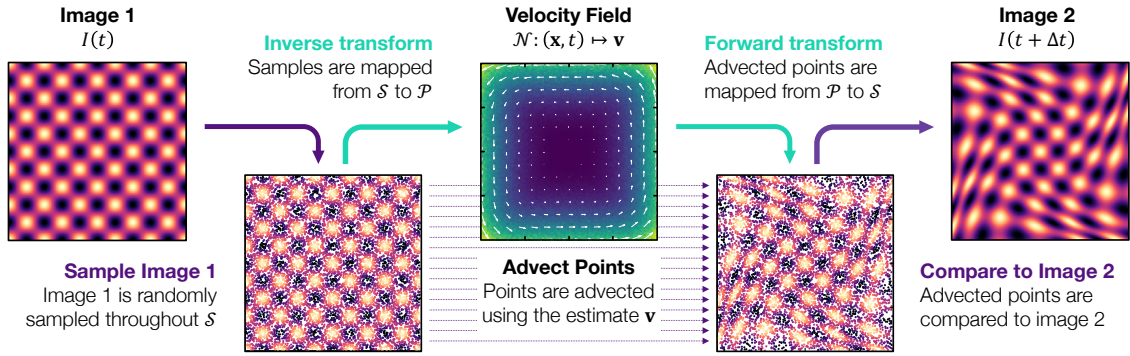


Figure 1: Schematic of the image warping procedure in NOF. Points are sampled in  $I(t)$ , advected to  $t + \Delta t$  by integrating  $\mathbf{v}$ , and then compared to the corresponding intensity in  $I(t + \Delta t)$ .

Our warping scheme involves five steps, illustrated in Fig. 1. First, a set of points is uniformly sampled from the sensor domain,  $\mathcal{S}$ . These points,  $\{\mathbf{s}_1, \mathbf{s}_2, \dots\}$ , are then mapped to world coordinates using the inverse camera transform,  $\mathbf{x}_i = \Psi^{-1}(\mathbf{s}_i)$ , as detailed in Appendix A. Next, the points are advected from  $\mathbf{x}_i$  to  $\mathbf{x}_i + \Delta\mathbf{x}_i$  using a forward Euler scheme to approximate the integral in Eq. (5a). Numerical integration of the continuous velocity field is crucial for managing large displacements; we use a time step of  $\Delta t/5$ , which proved stable across all tested flow scenarios, unless otherwise noted. Testing with a step size of  $\Delta t$  showed inferior accuracy compared to our multi-step approach. While this study uses a forward Euler scheme, future work may explore higher-order integration methods.

In the fourth step, the final locations of the points are transformed back to sensor coordinates using the camera transform,

$$\mathbf{s}_i + \Delta\mathbf{s}_i = \Psi(\mathbf{x}_i + \Delta\mathbf{x}_i). \quad (15)$$

Next, pixel intensities are sampled from the first image at  $\mathbf{s}_i$  and from the second image at  $\mathbf{s}_i + \Delta\mathbf{s}_i$ . When the displacement field is accurate, these intensity values should match. Intensities are retrieved via interpolation of the discrete image data:  $\mathbf{I} = \{I_{ij} \mid i = 1, \dots, m, j = 1, \dots, n\}$ , where  $I_{ij}$  is the intensity of the  $(i, j)$ th pixel in an  $m \times n$  image. While both bilinear and bicubic interpolation schemes were tested, bilinear interpolation is used throughout this work due to its lower computational cost and comparable accuracy across all cases. The interpolation operator is defined as

$$\mathcal{B}: [\mathbf{I}(t), \mathbf{s}] \mapsto \hat{I}(\mathbf{s}, t), \quad (16)$$

where  $\hat{I}$  is the interpolated estimate of the continuous intensity field,  $I$ . Further details about the interpolation scheme are provided in Appendix C.

Lastly, in the fifth step, we use Monte Carlo sampling to evaluate an integral-form data loss,

$$\mathcal{J}_{\text{data}}^k = \frac{1}{|\mathcal{S}_k|} \int_{\mathcal{S}_k} \{\mathcal{B}[\mathbf{I}(t), \mathbf{s}] - \mathcal{B}[\mathbf{I}(t + \Delta t), \mathbf{s} + \Delta \mathbf{s}_k]\}^2 d\mathbf{s},$$

where  $k$  denotes the camera index (to allow for multi-camera setups),

$$\Delta \mathbf{s}_k = \Psi_k \left[ \Psi_k^{-1}(\mathbf{s}) + \Delta \mathbf{x}_k \right] - \mathbf{s},$$

and  $\Delta \mathbf{x}_k$  is the solution to Eq. (5a) initialized at  $\Psi_k^{-1}(\mathbf{s})$ . For planar imaging, only a single camera is used, and the camera index can be omitted. However, capturing out-of-plane velocity components requires multiple cameras or auxiliary devices, such as endoscopes or fibers. In such cases, a separate data loss must be computed for each image, as discussed in the next section.

### 2.3 Data Loss for Stereo PIV

Three-dimensional effects are common in turbulent flows, vortex-dominated flows, unstable shear flows, and more. Stereoscopic PIV (stereo PIV) uses two cameras to simultaneously capture particles within the measurement plane from distinct perspectives. Data from these views allow for the extraction of out-of-plane fluid motion and helps to reduce perspective errors in the planar motion [55]. This two-dimensional, three-component (2D3C) velocimetry technique has become essential for accurately measuring velocity in flows with significant vortical content or other out-of-plane motions.

Most stereo PIV setups follow a translational or rotational configuration [56]. Figure 2 shows a graphical overview of planar and stereo PIV. In the translational version, both cameras have parallel optical axes that are perpendicular to the laser sheet. This setup is easy to implement, provides uniform magnification across the region of interest, and ensures a sharp focus, similar to single-camera planar PIV. However, the cameras in this configuration have a limited “common area” (i.e., the region of the laser sheet visible to both cameras). Expanding this area requires either (1) moving the two cameras closer, which sacrifices the accuracy of estimating out-of-plane motion, or (2) translating the sensors relative to the lenses, which can be challenging with many commercial cameras. Additionally, lens vignetting becomes more pronounced as the sensors move off-axis, especially at the large offsets needed for accurate out-of-plane motion estimation.

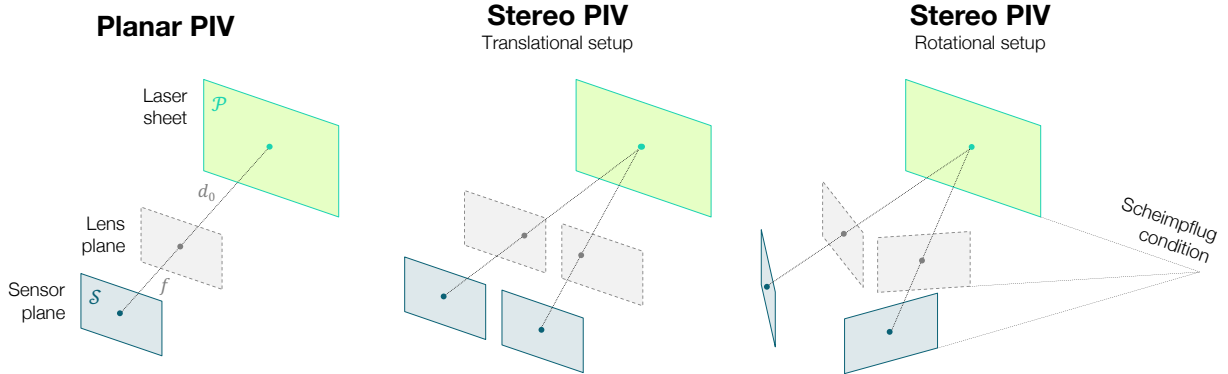


Figure 2: PIV setups: (left) planar, (middle) translational stereo, and (right) rotational stereo. Green planes are the laser sheet, cobalt planes are the sensors, and gray planes are the lenses. Diagram is not to scale.

The rotational setup addresses these challenges by turning both cameras to point them towards the center of the region of interest. Scheimpflug adapters are typically used to maintain a sharp focus from these oblique angles. This configuration overcomes the off-axis angle limitations of the translational method, reducing vignetting and enabling accurate out-of-plane motion estimation over a larger area. However, rotational setups introduce non-uniform magnification across the field of view, which complicates camera calibration and data processing. Both configurations are discussed in detail by Prasad [56].

In this work, we demonstrate NOF using the translational configuration for simplicity. However, our algorithm is equally applicable to the rotational configuration with appropriate adjustments to the camera transform. Details of the translational and rotational transforms are provided in Appendix A.4.

Traditional stereo PIV processing computes a displacement field for each perspective using OF, CC, or a similar technique. These fields are then mapped onto the laser plane in world coordinates, enabling the estimation of both in-plane and out-of-plane motion, as described by Eq. (48) in Appendix A.4. In contrast, stereo NOF performs the inversion directly in world space. Our stereo data loss follows the same structure as Eq. (17), with points sampled on the sensors, transformed into world coordinates, advected, and then mapped back to image space. The key difference is that stereo NOF forms a stereo data loss, with one component per camera, using their respective forward and inverse camera transforms:

$$\mathcal{J}_{\text{data}} = \mathcal{J}_{\text{data}}^{\text{L}} + \mathcal{J}_{\text{data}}^{\text{R}}. \quad (18)$$

Here,  $\mathcal{J}_{\text{data}}^{\text{L}}$  and  $\mathcal{J}_{\text{data}}^{\text{R}}$  are losses for the left and right cameras, respectively, which have different  $\Psi$  and  $\Psi^{-1}$  operators.

Although our measurement is planar, advection by the 2D3C velocity field can move points out of the plane/laser sheet. In principle, sampling of the network  $\mathcal{N}$  could be performed throughout a thin volume surrounding the laser sheet, within which particles are illuminated by a Gaussian laser slab of finite thickness. However, in our tests, sampling within the central  $x_1-x_2$  plane yielded the best results. Future work will explore improved sampling schemes to more accurately capture out-of-plane effects.

## 2.4 Physics-Inspired Regularization

An explicit penalty term is often included in the aggregate loss to close the OF equations and promote desirable solution characteristics. Most OF regularization methods use “physics-inspired” penalties that do not strictly align with the governing equations but encourage properties like smoothness or a known correlation length scale [57]. NOF can apply the same penalty terms as other OF algorithms for PIV but does so in a *truly* continuous form. For comparison, WOF relies on gradient operators tied to the discrete signal space associated with the wavelet transform. Moreover, we regularize the flow velocity within the measurement plane in world space,  $\mathcal{P}$ , rather than sensor space. This ensures consistent regularization for stereo PIV and facilitates the more comprehensive, physics-based penalties discussed in the next section.

A common penalty choice is the *first-order* Tikhonov regularization method introduced to OF by Horn and Schunck [53],

$$\mathcal{J}_{\text{penalty}} = \frac{1}{|\mathcal{P}|} \int_{\mathcal{P}} \|\nabla_{\mathbf{x}} \mathbf{v}\|_2^2 \, \mathrm{d}\mathbf{x}, \quad (19)$$

where  $\|\cdot\|_2$  is the Euclidean norm. Tikhonov regularization promotes *globally* smooth solutions in the  $L^2$  sense. Another common choice is total variation (TV) regularization, which minimizes the overall gradient content to promote *piecewise* smooth solutions that can sustain sharp discontinuities, i.e., enforcing smoothness in the  $L^1$  sense:

$$\mathcal{J}_{\text{penalty}} = \frac{1}{|\mathcal{P}|} \int_{\mathcal{P}} \|\nabla_{\mathbf{x}} \mathbf{v}\|_1 \, \mathrm{d}\mathbf{x}. \quad (20)$$

Note that  $\|\cdot\|_1$  is the Manhattan norm, which is non-differentiable and typically requires a specialized optimization technique. Higher-order regularization terms, such as

$$\mathcal{J}_{\text{penalty}} = \frac{1}{|\mathcal{P}|} \int_{\mathcal{P}} \left( \frac{\partial^3 v_1}{\partial x_1^3} \right)^2 + \left( \frac{\partial^3 v_2}{\partial x_2^3} \right)^2 \, \mathrm{d}\mathbf{x} \quad (21)$$

can improve velocity estimation without excessively smoothing the field or penalizing divergence and curl [8, 23, 24]. A particularly effective approach for 2D velocity fields is div-curl regularization,

$$\mathcal{J}_{\text{penalty}} = \frac{1}{|\mathcal{P}|} \int_{\mathcal{P}} \|\nabla_{\mathbf{x}} (\nabla_{\mathbf{x}} \cdot \mathbf{v})\|_2^2 + \|\nabla_{\mathbf{x}} (\nabla_{\mathbf{x}} \times \mathbf{v})\|_2^2 \, \mathrm{d}\mathbf{x}, \quad (22)$$

which aims to smooth the flow by penalizing gradients of divergence and curl while preserving the structure of vortical and compressive regions [19, 24, 54, 58].

Penalizing higher-order derivatives in an explicit penalty term often introduces numerical sensitivities that challenge optimization algorithms and increase computational costs. In NOF, the network architecture provides implicit regularization, as outlined in Appendix B. Adjusting the Fourier encoding influences the

spectral content that the neural network can learn. The bandwidth of the network may be tailored to the flow, e.g., based on an estimated Reynolds number or known spectral properties [59]. Systematic testing demonstrated that implicit regularization is both more accurate and efficient than explicit methods in NOF. Therefore, we employ implicit regularization throughout this work unless we state otherwise.

## 2.5 Physics-Based Constraints

Explicit physics-based constraints enhance the accuracy and physical consistency of solutions. While some constraints can be applied in other OF methods, such as mass continuity for incompressible flows [19, 60, 61], NOF offers distinct advantages. Specifically, our approach enables time-resolved reconstructions that include the Navier–Stokes equations. Additionally, NOF’s space–time representation allows us to exploit sparsity in the time domain: an advantage not utilized by existing OF methods.

Many flows are incompressible, making it advantageous to represent the velocity field in a way that inherently satisfies the continuity equation,

$$\frac{\partial \rho}{\partial t} + \nabla_{\mathbf{x}} \cdot (\rho \mathbf{v}) = 0 \Rightarrow \nabla_{\mathbf{x}} \cdot \mathbf{v} = 0. \quad (23)$$

This is straightforward to implement in NOF. For example, a 2D divergence-free velocity field can be represented using a scalar potential,  $\varphi$ , where  $\mathcal{N} : (\mathbf{x}, t) \mapsto \varphi$  and

$$\mathbf{v} = \left( -\frac{\partial \varphi}{\partial y}, \frac{\partial \varphi}{\partial x} \right). \quad (24)$$

Taking the divergence of this field confirms compliance with the continuity equation,

$$\nabla_{\mathbf{x}} \cdot \mathbf{v} = -\frac{\partial^2 \varphi}{\partial x \partial y} + \frac{\partial^2 \varphi}{\partial y \partial x} = 0. \quad (25)$$

Although this approach is limited to 2D flows, continuity can still be embedded as a hard constraint in 3D settings via a vector potential field,

$$\boldsymbol{\varphi} = (\varphi_1, \varphi_2, \varphi_3). \quad (26)$$

The network maps  $(\mathbf{x}, t)$  to  $\boldsymbol{\varphi}$  and the velocity field is given by

$$\mathbf{v} = \nabla_{\mathbf{x}} \times \boldsymbol{\varphi}, \quad (27)$$

ensuring, again, that the velocity field remains divergence-free,

$$\nabla_{\mathbf{x}} \cdot (\nabla_{\mathbf{x}} \times \boldsymbol{\varphi}) = 0. \quad (28)$$

In practice, two components of  $\boldsymbol{\varphi}$  may be sufficient, with  $\varphi_3 = 0$ . Further research is needed to assess this approach for 3D3C measurements, such as tomographic PIV [3] and Lagrangian particle tracking [13].

In addition to hard constraints, we incorporate soft constraints by including the residuals of the 2D Navier–Stokes equations to enable *direct* time-resolved pressure estimation from PIV data for 2D flows:

$$\mathcal{J}_{\text{penalty}} = \frac{1}{|\mathcal{P} \times \mathcal{T}|} \int_{\mathcal{T}} \int_{\mathcal{P}} \underbrace{(\nabla_{\mathbf{x}} \cdot \hat{\mathbf{v}})^2}_{\text{continuity}} + \underbrace{\left\| \frac{\partial \hat{\mathbf{v}}}{\partial t} + \hat{\mathbf{v}} \cdot \nabla_{\mathbf{x}} \hat{\mathbf{v}} + \nabla_{\mathbf{x}} \hat{p} - \frac{1}{Re} \nabla^2 \hat{\mathbf{v}} \right\|_2^2}_{\text{momentum conservation}} \mathrm{d}\mathbf{x} \mathrm{d}t. \quad (29)$$

In this expression,  $\mathcal{T}$  is the time domain of the experiment, while  $\hat{\mathbf{v}} = \mathbf{v}/v_0$  and  $\hat{p} = p/(\rho_0 u_0^2)$  represent the dimensionless velocity and pressure, respectively, and  $v_0$ ,  $\rho_0$ , and  $\ell_0$  are the characteristic velocity, density, and length scales. The reference Reynolds number is

$$Re = \frac{\rho_0 u_0 \ell_0}{\mu}. \quad (30)$$

Note that the mass continuity residuals in Eq. (29) are redundant when using one of the hard constraints presented above. Incorporating governing equation residuals into the loss effectively transforms NOF into a PINN, where the estimated velocity field not only aligns with PIV data but also approximately solves the Navier–Stokes equations. This enhances the accuracy of velocity estimates and enables simultaneous pressure inference. However, it only applies to 2D flows, as planar cross-sections of fully-3D flows do not satisfy the 2D equations, and there is too much uncertainty for a 3D solution. In such cases, 3D measurements are required for effective data assimilation [62, 63].

### 3 Flow Scenarios and Metrics

We evaluate NOF across a range of synthetic and experimental scenarios. The synthetic cases provide idealized, noise-free conditions to assess accuracy under varying seeding densities and examine the effects of out-of-plane motion using both 2D and 3D flows. The experimental cases offer a more realistic test of NOF’s performance under conditions with noise, shot-to-shot laser intensity variations, and non-uniform seeding and illumination. Sample images for each scenario are shown in Fig. 3, with detailed descriptions provided in the following sections.

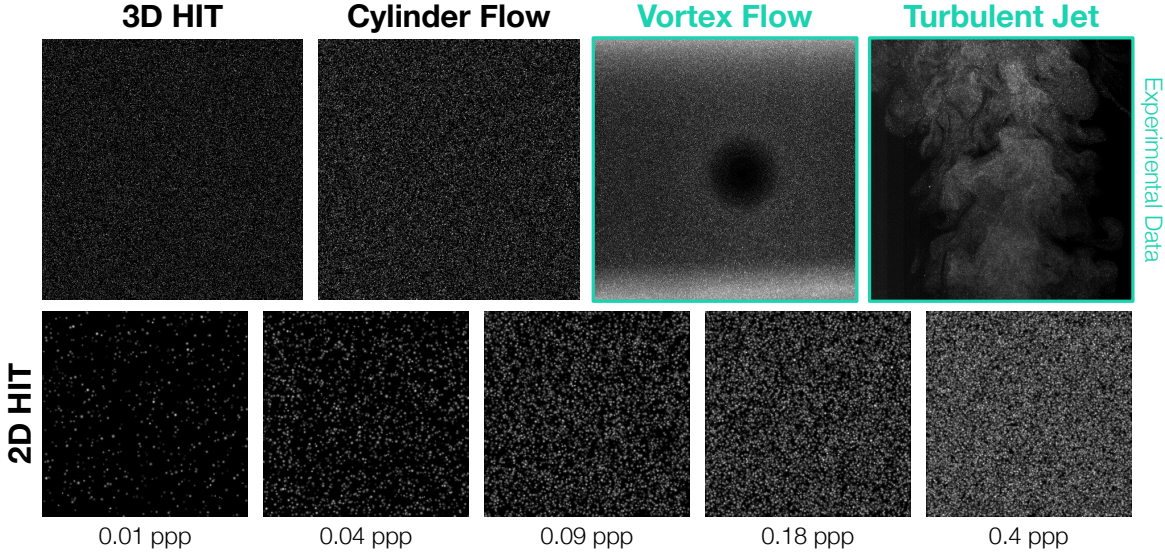


Figure 3: Sample particle images from synthetic and experimental flow cases. Experimental cases from previous PIV challenges [64, 65] are highlighted with a teal border.

#### 3.1 Synthetic Cases

We use three DNS datasets for synthetic testing: 2D homogeneous isotropic turbulence (HIT) from Carlier and Wieneke [66], 3D HIT from the Johns Hopkins Turbulence Database [67], and a 3D cylinder wake flow from Raissi et al. [40]. These cases, referred to as 2D HIT, 3D HIT, and cylinder flow, contain 100, 51, and 201 frames, respectively.

Table 1: Parameters and Dimensions of the DNS Flow Cases

Flow case	$Re$	Domain size		Time step		Grid
		DNS	dim., mm	DNS	dim., ms	
2D HIT	3000	$2\pi \times 2\pi$	$100 \times 100$	0.01	0.845	$256 \times 256$
3D HIT	5405	$2\pi \times 2\pi \times 5\pi/64$	$150 \times 150 \times 5.9$	0.002	0.211	$1024 \times 1024 \times 40$
Cylinder	100	$5 \times 5 \times 5$	$5 \times 5$	0.08	0.80	$51 \times 51 \times 51$

To mimic realistic flow imaging conditions, we dimensionalize each dataset under the assumption that the fluid is water. The hypothetical setups are designed to conform to typical PIV configurations. Table 1 summarizes key dimensionless and dimensional quantities for each scenario, with Reynolds numbers defined using the energy injection scale (2D and 3D HIT) or the cylinder diameter.

Generating synthetic particle images involves numerically advecting tracer particles and projecting their position into sensor space. As outlined in Appendix A, we assume a pinhole camera with a magnification of 1/3. Object distances are set to 120, 150, and 60 mm for the 2D HIT, 3D HIT, and cylinder cases, respectively, with focal lengths of 40, 50, and 20 mm. For planar setups, the image plane is coincident with the physical  $x_1-x_2$  plane and the camera is centered at  $x_1 = x_2 = 0$  mm. The inter-lens spacing is set to 75 mm in our stereo 3D HIT test. In all scenarios, the synthetic laser sheet has a Gaussian profile that straddles  $x_3 = 0$  mm, with a standard deviation in the  $x_3$ -direction of 0.63 mm.

Particles are seeded uniformly throughout the physical domain and advected according to the velocity field. For the 3D HIT and cylinder flows, we employ a second-order Runge–Kutta scheme, while for 2D HIT, we use a forward Euler scheme with at least 50 steps per frame. Periodic boundary conditions are applied to the HIT cases. For the cylinder flow, particles exiting the domain are re-injected at the opposite boundary at a randomized height. Particle locations are projected onto the image plane using Eq. (44a) for planar setups and Eq. (46) for stereo setups. Image resolutions are matched to the grid sizes listed in Table 1, except for the cylinder case where images of  $841 \times 841$  px are synthesized. Particles are modeled as Gaussian blobs with a standard deviation of 1.25 pixels, giving them an apparent diameter of 3–4 pixels. For 2D HIT, the particle density is varied from 0.01 to 0.4 ppp to assess the effects of seeding density.

A key advantage of synthetic testing is the availability of ground truth data, allowing for precise error quantification. For our analysis, we report normalized root-mean-square errors (NRMSEs) of the fluctuating components. This metric allows us to assess whether each technique can capture unsteady flow behavior, as the mean components are relatively easy to estimate. For a quantity of interest  $g$ , we apply a Reynolds decomposition,  $g = \bar{g} + g'$ . The NRMSE for  $g$  is

$$e_g = \frac{\langle \|g' - g'_{\text{exact}}\|_2 \rangle}{\langle \|g'_{\text{exact}}\|_2 \rangle} \quad (31)$$

where  $g'_{\text{exact}}$  is the exact fluctuating component and  $\langle \cdot \rangle$  indicates a spatial average over the measurement domain,

$$\langle g \rangle = \frac{1}{|\mathcal{P}|} \int_{\mathcal{P}} g(\mathbf{x}) \, d\mathbf{x}. \quad (32)$$

In our Reynolds decomposition,  $\bar{g}$  is the time average of  $g$  over the measurement interval.

### 3.2 Experimental Cases

We also demonstrate NOF on two experimental datasets: a strong vortex flow from the first international PIV challenge [64] and a time-resolved jet flow from the third challenge [65]. These cases are referred to as vortex flow and turbulent jet flow, respectively.

The vortex flow dataset [64] consists of two consecutive frames capturing a vortex formed behind the wingtip of a transport aircraft (ALVAST half-model) in a landing configuration. The main air flow is perpendicular to the laser plane, with a velocity of  $60 \text{ m s}^{-1}$ , and the measurement plane is positioned 1.64 m behind the wingtip. Images are taken with a progressive scan camera featuring a  $1024 \times 1280$  px chip and  $6.7 \times 6.7 \text{ }\mu\text{m}$  pixels. We crop the images to  $1024 \times 1024$  px, reducing the field of view from  $140 \times 170 \text{ mm}^2$  to  $140 \times 140 \text{ mm}^2$ . The magnification is approximately 0.05. Since the frame rate is not specified, we follow the original PIV challenge paper and report results in pixels-per-frame (ppf). This dataset is characterized by strong intensity gradients, a non-uniform particle density, and particle size variations, which pose significant challenges for PIV algorithms, making it an excellent test of NOF’s robustness.

The turbulent jet flow dataset [65] features a nitrogen jet with an exit velocity of approximately  $30 \text{ m s}^{-1}$ . The nozzle has a diameter of 5 mm, and the flow is seeded with oil-mist particles averaging  $5 \text{ }\mu\text{m}$  in diameter. The domain is illuminated with 527 nm light from a high-speed dual-head PIV laser (New Wave Pegasus) operating at 5 kHz and imaged with a high-speed camera (Photron APX-RS). The camera has a  $512 \times 512$  px sensor,  $17 \times 17 \text{ }\mu\text{m}$  pixels, and magnification of 0.3 for the PIV plane. Imaging is performed at 10 kHz using frame straddling to capture the output of both laser heads, which have an inter-frame time separation of  $10 \text{ }\mu\text{s}$ . This dataset was selected to evaluate NOF’s ability to handle noise and inter-frame intensity variations, which are common complications in a PIV experiment.

## 4 Synthetic Results

This section evaluates the performance of NOF across multiple synthetic flow cases, comparing it to CC and WOF methods. Throughout these tests, we perform CC with a standard cascade over  $64^2$ -,  $32^2$ -, and  $16^2$ -pixel interrogation windows with aggressive overlapping of 75%. WOF hyperparameters are *optimally* tuned for each case. We explore several NOF variants with distinct regularization schemes and flow parameterizations, first testing their performance on the 2D HIT case under different seeding densities. Spectral error analysis provides additional insights into how well each method captures different flow scales. Next, we demonstrate NOF’s accuracy and flexibility with both planar and stereo PIV configurations on 3D HIT

data, where strong out-of-plane motion is present. Finally, we showcase NOF's ability to recover pressure fields directly from planar PIV measurements in the cylinder flow case.

#### 4.1 2D HIT

We begin with the results of the 2D HIT test. Figure 4 compares the ground truth DNS data to the reconstructed fields obtained from CC, WOF, and NOF. The vanilla implementation of NOF, which employs implicit regularization as described in Sec. 2.4, performs single-shot reconstructions using a pair of particle images. These results were obtained at a seeding density of 0.17 ppp, a typical value in PIV experiments. This density avoids severe particle overlap, as shown in Fig. 3, while remaining sufficient to resolve the Taylor micro-scale of turbulence, as can be seen in Fig. 5.

Qualitatively, both NOF and WOF recover the velocity field with high accuracy, showing strong similarity to the ground truth, while CC introduces visible low-pass filtering. This trend is further confirmed by the absolute errors shown at the bottom of Fig. 4, where WOF and NOF yield minimal errors compared to CC. Notably, WOF exhibits slightly more artifacts than NOF, particularly near the boundaries. This is consistent with observations in the experimental jet case in Sec. 5.2, shown in Fig. 16. Quantitatively, NRMSEs for the velocity magnitudes are 17.3%, 6.2%, and 5.1% for CC, WOF, and NOF, respectively.

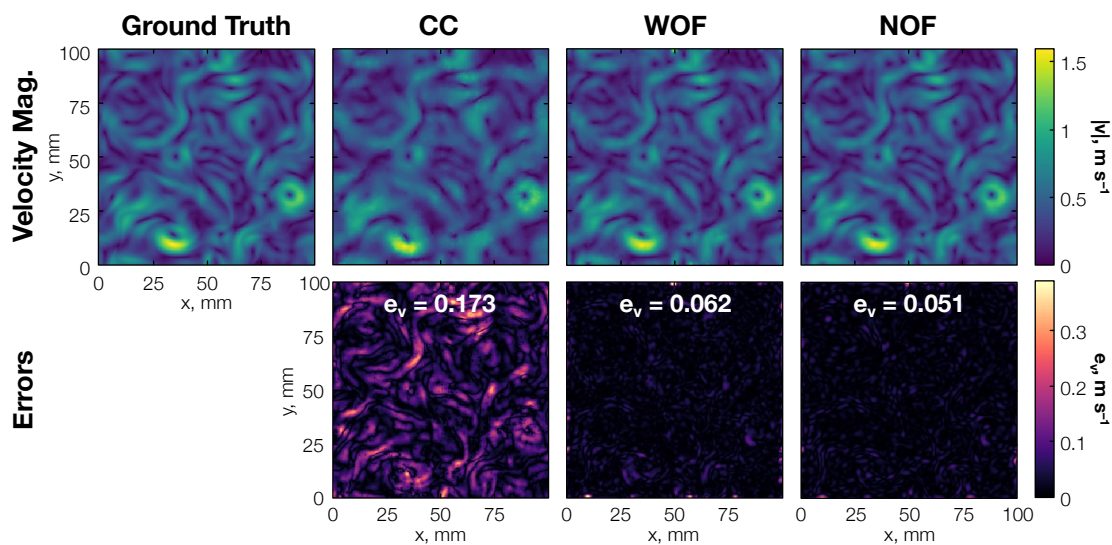


Figure 4: Exact and reconstructed 2D HIT velocity magnitude fields (top) and absolute point-wise errors (bottom). NRMSEs are superimposed on the absolute error plot.

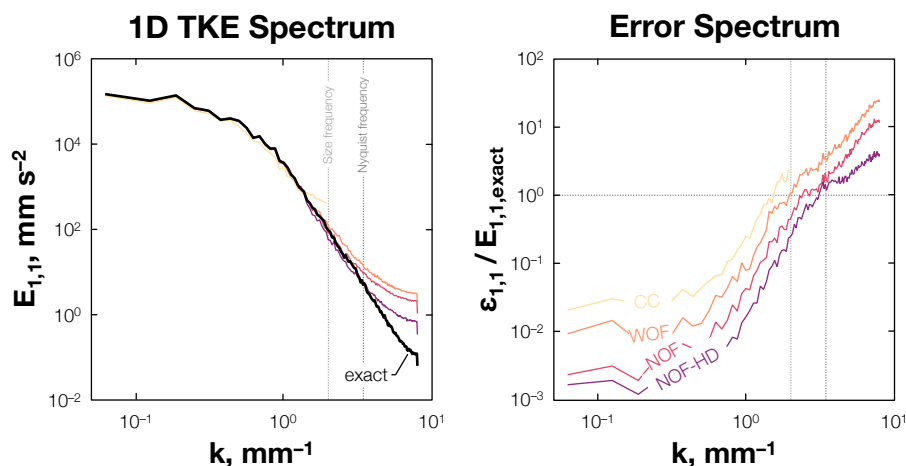


Figure 5: Comparison of 1D TKE spectra of flows reconstructed by different methods and exact DNS data (left) and normalized error spectra (right).

While NRMSEs provide an overall measure of flow accuracy across the domain, spectral analysis offers deeper insights into the performance of each method at different length scales. Figure 5 shows 1D turbulent kinetic energy (TKE) spectra,  $E_{1,1}$ , for velocity fields reconstructed by CC, WOF, NOF, and NOF-HD. The NOF-HD variant adds a hard constraint to enforce mass continuity, as described in Sec. 2.5.

To interpret trends in the error spectra, we define the particle size and spacing-Nyquist frequencies,

$$\kappa_p = \frac{2\pi}{d_p} \quad \text{and} \quad \kappa_N = \frac{\pi}{\ell_p}, \quad (33)$$

respectively, where  $d_p$  is the apparent particle diameter on the sensor projected into physical space and  $\ell_p$  is the mean inter-particle spacing. Specifically,  $\kappa_p$  represents the spatial frequency associated with the particle image size, below which flow features are obscured by the particle. Meanwhile,  $\kappa_N$  indicates the maximum recoverable frequency for a given seeding density, following the Shannon–Nyquist sampling theorem [68].

We hypothesize that, absent physics-based constraints, the accuracy of OF methods is fundamentally constrained by the lower of these frequencies, beyond which finer flow details cannot be resolved. As shown on the left side of Fig. 5, CC deviates from the ground truth spectrum well before reaching the particle size frequency, due to the low cut-off imposed by its large interrogation window. By comparison, WOF and NOF closely match the ground truth spectrum up to the particle size frequency. Remarkably, NOF-HD surpasses this limit, maintaining accuracy up to the Nyquist frequency. This highlights the value of incorporating physical constraints into OF algorithms, enabling better resolution of fine-scale flow features.

Spectral errors for each method are normalized by the flow’s true kinetic energy at that wavenumber,  $\varepsilon_{1,1}/E_{1,1,\text{exact}}$ . This metric captures the reconstruction accuracy across different length scales, as shown on the right side of Fig. 5. Both NOF variants demonstrate superior reconstructions across the spectrum. All methods exhibit similar trends: low errors at small wavenumbers, followed by an exponential increase at higher wavenumbers. At the particle size frequency, CC and WOF reach nearly 100% error, while NOF-HD maintains an error close to 20%. Curiously, both WOF and the vanilla version of NOF show consistent exponential growth of errors at high wavenumbers. In contrast, NOF-HD exhibits a slower increase, especially beyond the Nyquist frequency, suggesting that enforcing mass continuity mitigates particle-induced artifacts and suppresses random errors at high frequencies. However, NOF-HD was not able to resolve flow behavior frequencies beyond  $\kappa_N$ .

Table 2: Errors for State-of-the-Art Motion Estimation Schemes

Regime	Algorithm					
	CC	WOF	NOF	NOF-HD	NOF-TR	NOF-phys
Sub-Nyquist	20.94	9.13	6.76	5.26	8.95	8.16
Super-Nyquist	N/A	188.42	134.78	114.12	141.47	106.22

To better assess the accuracy of flow reconstruction across resolved and unresolved scales (disregarding the finite particle image size), we compute *sub-* and *super-*Nyquist errors of the velocity fields, which are listed in Table 2. Sub-Nyquist errors are calculated by low-pass filtering the velocity field in the Fourier domain with a cut-off frequency at  $\kappa_N$ : all Fourier components with  $|\kappa| \geq \kappa_N$  are set to zero. The filtered field is reconstructed by the inverse Fourier transform, and sub-Nyquist errors are evaluated using Eq. (31). Super-Nyquist errors are similarly computed by high-pass filtering, where all components with  $|\kappa| < \kappa_N$  are zeroed out, with errors subsequently computed in the physical domain.

Table 2 provides sub- and super-Nyquist errors for the 2D HIT case reconstructed using CC, WOF, and several NOF variants. Two additional NOF variants are introduced at this stage: time-resolved NOF (NOF-TR) and physics-constrained NOF (NOF-phys). NOF-TR extends the single-shot NOF to a spatio-temporally resolved representation (2D +  $t$ ), while NOF-phys incorporates the 2D Navier–Stokes and continuity losses, as given in Eq. (29). Both NOF-TR and NOF-phys were trained on a sequence of 20 particle images, with the reported errors corresponding to the fifth frame to match the non-time-resolved tests.

Among all methods, WOF exhibits the highest super-Nyquist error, potentially due to artifacts introduced by regularization in the wavelet domain. The impact of NOF modifications is also evident: while NOF-TR shows slightly higher sub- and super-Nyquist errors, due to the increased data and sampling density constraints in the larger spatiotemporal domain, it achieves a 20-fold increase in data compression and

reduces training time per frame from 3–7 minutes to 20–45 seconds. More significantly, NOF-phys improves super-Nyquist accuracy beyond that achieved with the hard divergence constraint in NOF-HD. While the inclusion of Navier–Stokes residuals only marginally reduces sub-Nyquist errors, it substantially decreases super-Nyquist errors by mitigating spurious high-frequency artifacts. These results underscore the value of physics-based constraints, particularly for reducing non-physical fluctuations in the super-Nyquist regime.

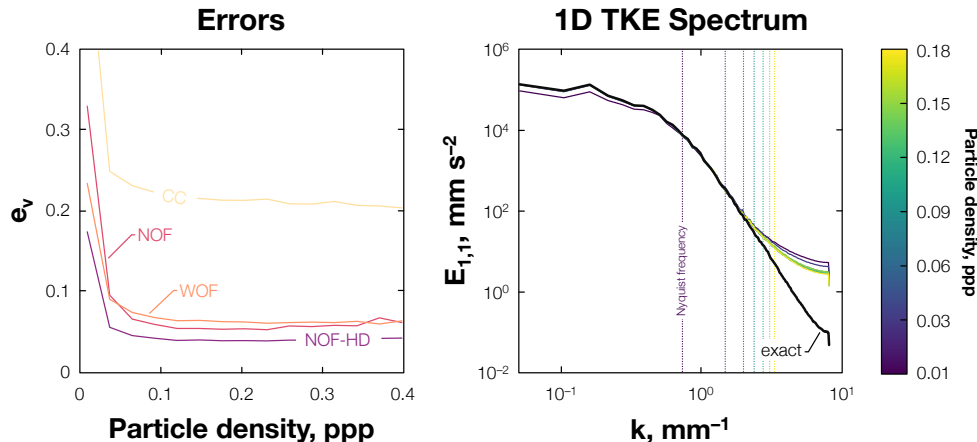


Figure 6: NRMSE of 2D HIT flow reconstructed by different methods under varying ppp (left) and the corresponding 1D TKE spectra of NOF reconstruction (right). Note that the NOF’s spectra overlap exactly with the ground truth spectrum at  $ppp > 0.03$ .

In addition to the tests at a fixed seeding density of 0.17 ppp, we evaluated the performance of CC, WOF, NOF, and NOF-HD across varying particle densities, with results shown in Fig. 6. Our analysis focuses on NOF and NOF-HD, as they represent the two core variants with favorable accuracy (see Table 2). The left plot in Fig. 6 depicts NRMSEs of velocity magnitude fields, averaged over ten consecutive snapshots, across a range of particle densities from 0.01 to 0.4 ppp. Exemplary snapshots at a range of particle densities can be seen in the bottom row of Fig. 3.

Once again, NOF outperforms WOF at all but the lowest seeding densities and consistently surpasses CC across the entire range. NOF-HD delivers the best overall performance, once again underscoring the benefits of imposing hard physical constraints for flow reconstruction. The right plot in Fig. 6 shows the 1D TKE spectra of NOF-reconstructed fields at various seeding densities. As expected, reducing the density diminishes low-wavenumber content while amplifying high-frequency noise. This effect arises because increased inter-particle spacing allows more spurious velocity oscillations between particles. Such oscillations are not penalized by the loss function when the particle spacing grows too large.

The plot also includes vertical lines marking the Nyquist frequency for each seeding density, which roughly aligns with the point at which the spectra diverge for ppp values below 0.06. Further increases in seeding density do not yield significant improvements in resolving finer flow scales, as the finite size of particles in the images becomes the limiting factor.

## 4.2 3D HIT

Both planar and stereo PIV configurations are applied to the 3D HIT flow case. While NOF achieves accuracy comparable to (or slightly better than) WOF in the planar setup, it robustly outperforms WOF in the stereo configuration, benefiting from the all-in-one flow reconstruction scheme introduced in Sec. 2.3. Notably, these tests use a forward Euler step size of  $\Delta t$  to reduce computational cost, as the dataset’s small, approximately linear deflections allow for this simplification.

### 4.2.1 Planar PIV

Figure 7 compares the ground truth DNS velocity magnitude field to CC, WOF, and vanilla NOF reconstructions. The 3D HIT dataset presents greater challenges than the 2D HIT flow in Sec. 4.1 due to its high dynamic range and rich spectral content. Complex flow features in the measurement plane impact the performance of all three methods, with NRMSE values of 19.5%, 13.3%, and 13.1% for CC, WOF, and NOF, respectively. While WOF and NOF achieve similar levels of accuracy, both methods smooth out some fine-scale features present in the true field. Note that WOF *appears* to retain veridical high-frequency content

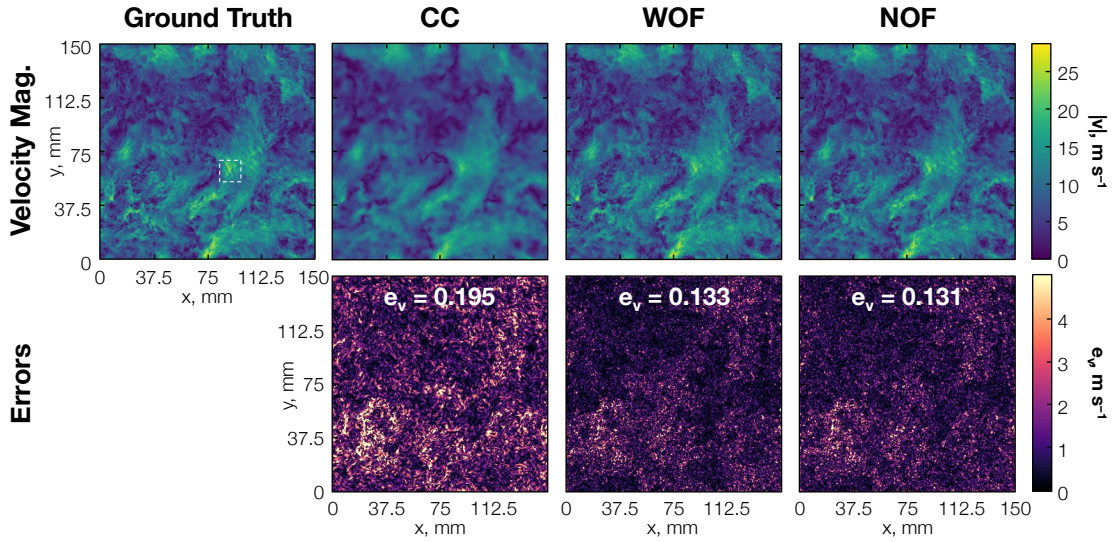


Figure 7: Exact and reconstructed 2D2C velocity magnitude fields of 3D HIT with a planar setup (top) and absolute point-wise errors (bottom). NRMSEs are superimposed on the absolute error plot.

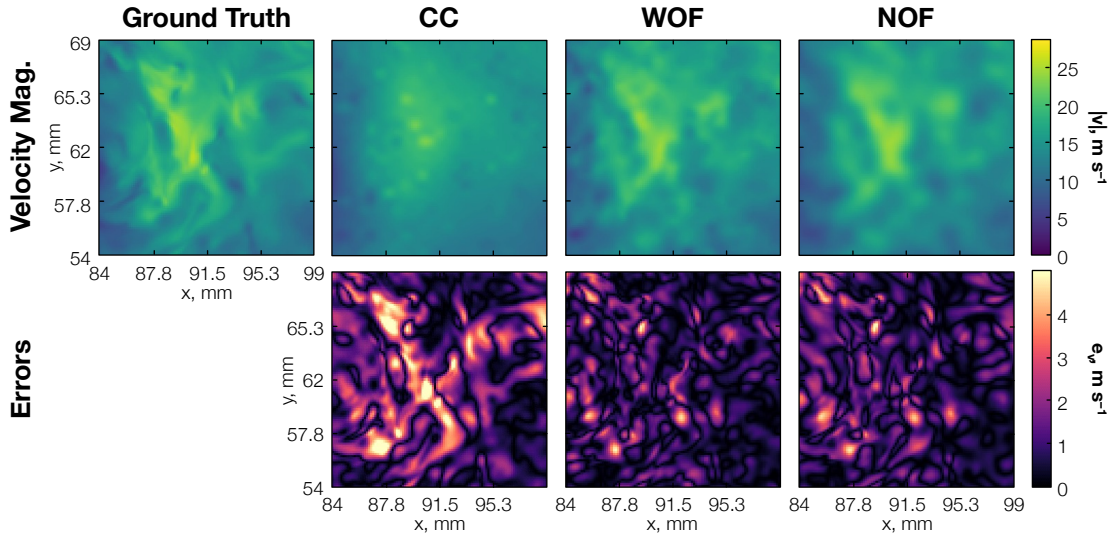


Figure 8: Zoomed views of the 2D2C velocity magnitude fields outlined by the white box in Fig. 7 (top) and the absolute point-wise errors (bottom).

compared to NOF. Figure 8 shows a zoomed-in view of the region highlighted by the dashed white square in Fig. 7, revealing spurious, unresolved features in WOF’s reconstruction. In contrast, NOF provides a smoother reconstruction due to the implicit regularization of the neural network. These close-ups also emphasize the limitations of CC: the distinctive “X” shaped feature in the ground truth field is entirely missing from the CC estimate. While certain CC methods are capable of resolving finer structures, the version used here represents the most common and widely adopted approach [7–13, 24, 69].

Figure 9 presents 1D TKE and normalized error spectra for CC, WOF, NOF, and NOF-TR (evaluated over 20 frames), similar to the analysis in Fig. 5 for 2D HIT. All methods exhibit spectral deviations from the ground truth before reaching the Nyquist frequency, indicating their limited ability to fully capture or measure the flow’s dynamics at high frequencies. Although WOF diverges from the ground truth later than NOF and NOF-TR, this delayed divergence is accompanied by higher errors, as shown in the right plot. Overall, the normalized error spectra indicate that NOF and WOF demonstrate comparable representational quality across most of the frequency range. However, notable differences emerge at the frequency extremes (low and high frequencies), where NOF methods are significantly better than the alternatives.

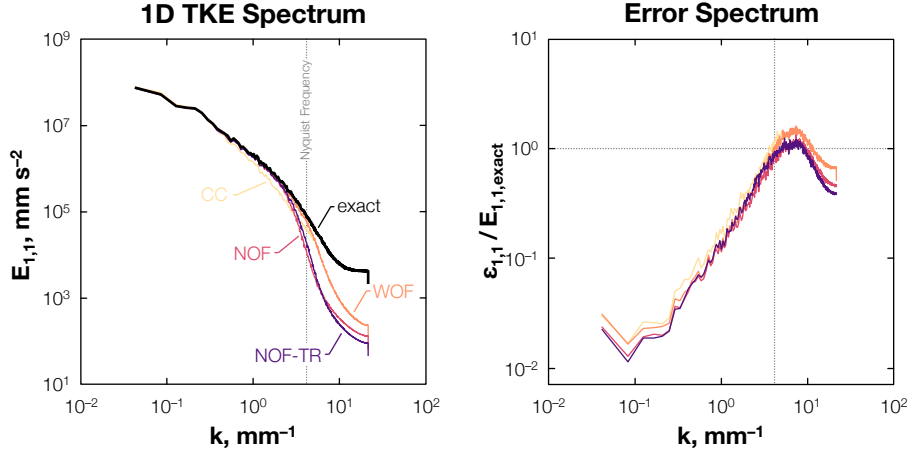


Figure 9: Comparison of 1D TKE spectra of reconstructed 2D2C velocity field from a 3D HIT and exact DNS data (left) and normalized error spectra (right).

#### 4.2.2 Stereo PIV

Neural optical flow offers a unique integrated approach for stereo flow reconstruction in which a single 3D velocity field is sought to simultaneously minimize both OF data losses. Figure 10 compares the velocity magnitude fields of the ground truth DNS to CC, WOF, and vanilla NOF. Unlike CC and WOF, which combine two separate 2D2C displacement fields into a single 2D3C field using Eq. (48), NOF directly reconstructs the physical displacement field through a stereo data loss defined in Eq. (18). The resulting NRMSEs are 18.4%, 17.6%, and 13.9% for CC, WOF, and NOF, respectively.

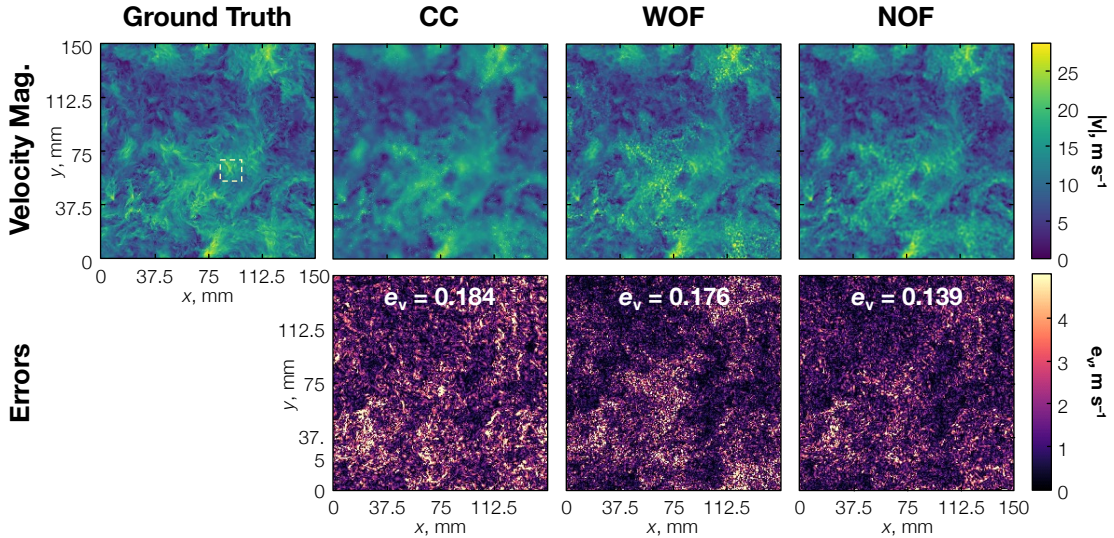


Figure 10: Exact and reconstructed 2D3C velocity magnitude fields of 3D HIT with a stereo setup (top) and absolute point-wise errors (bottom). NRMSEs are superimposed on the absolute error plot.

Compared to the planar tests in Sec. 4.2.1, WOF shows a significant increase in error (from 13.3% to 17.6%), highlighting its limitations in stereo configurations for capturing out-of-plane motion. By comparison, NOF experiences only a minor increase in error (from 13.1% to 13.9%), demonstrating its robustness in stereo analysis. Higher errors from WOF are likely due to the recombination step in traditional stereo PIV, which amplifies artifacts in the 2D2C estimates. As in Sec. 4.2.1, WOF may appear to resolve finer details than NOF, but these details are often spurious. Figure 11 provides close-ups of the fields, highlighting artifacts in the WOF estimate near the left boundary. Comparing these close-ups with Figs. 8 and 11 further illustrates how the out-of-plane velocity component amplifies these artifacts.

Figure 12 provides a rigorous evaluation of spectral content through the 1D TKE and normalized error

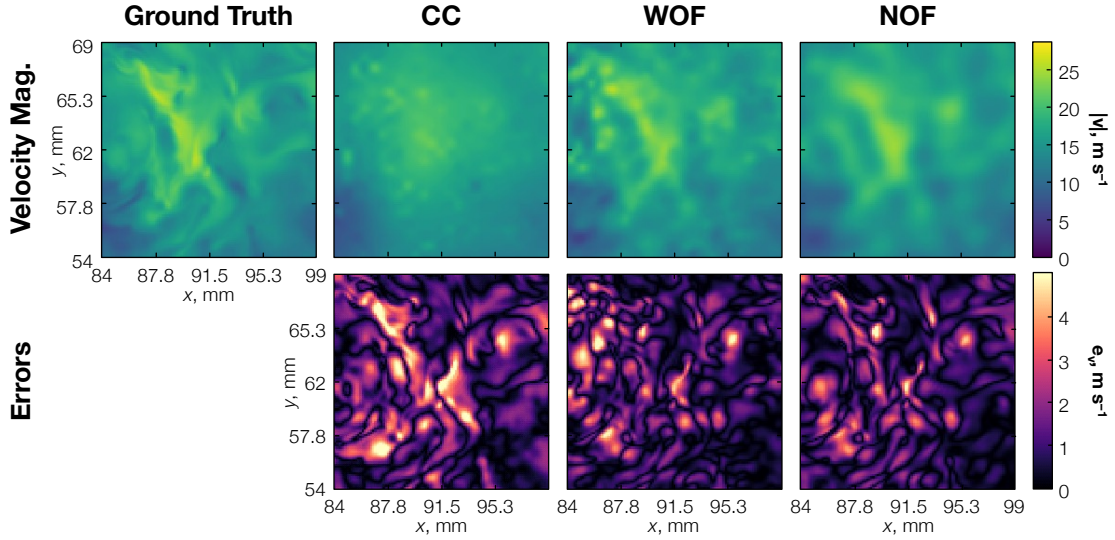


Figure 11: Zoomed views of the 2D3C velocity magnitude fields outlined by the white box in Fig. 10 (top) and the absolute point-wise errors (bottom).

spectra for the  $v_1$  (horizontal) and  $v_3$  (out-of-plane) velocity components. Given that the spectral behavior of the two in-plane components,  $v_1$  and  $v_2$  (vertical), is nearly identical, only  $v_1$  is shown. This figure includes NOF-TR alongside CC, WOF, and vanilla NOF for comparison. The normalized error spectra reveal a consistent reduction in error across all three velocity components with NOF compared to CC and WOF. For the in-plane components,  $v_1$  and  $v_2$ , error reductions are particularly evident at high frequencies, indicating improved resolution of fine-scale flow features. Notably, the largest error reduction is seen in the out-of-plane component,  $v_3$ , where NOF lowers errors across the entire frequency range. These results highlight NOF's superior ability to capture out-of-plane motion accurately, an advantage that becomes especially valuable in complex 3D flow scenarios.

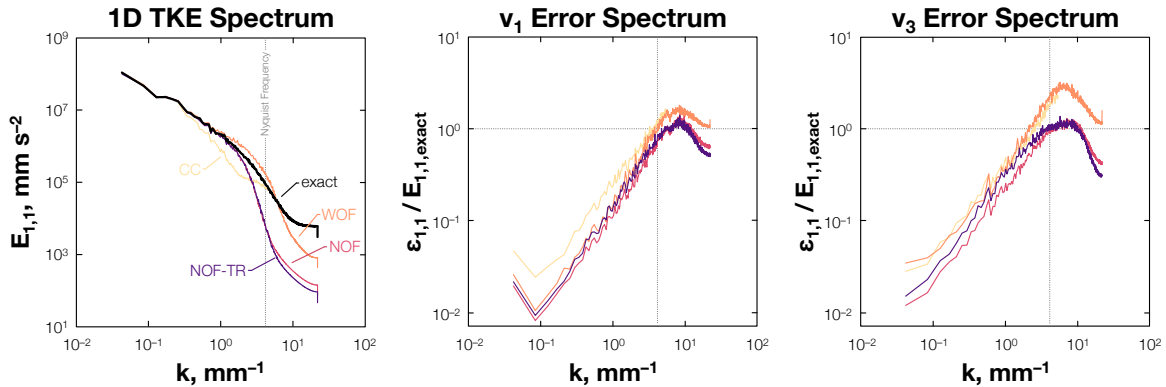


Figure 12: Comparison of 1D TKE spectra of reconstructed 2D3C velocity field from a 3D HIT and exact DNS data (left) and normalized error spectra for the  $v_1$  (middle) and  $v_3$  components (right).

A key objective of stereo NOF is to enable pressure recovery from PIV in complex 3D flows. However, in this 3D HIT case, the absence of out-of-plane velocity gradients prevents accurate pressure estimation. Similarly, without  $\partial v_3 / \partial x_3$  information, the continuity constraint could become inadequate. The physics-informed NOF variants (NOF-HD and NOF-phys) are thus omitted from this analysis. Both NOF and NOF-TR diverge from the ground truth spectrum at the same frequency as WOF, but their spectral content decays more rapidly beyond this point, likely due to limited expressivity of the networks.

### 4.3 Cylinder Flow

In this section, we present results from our cylinder flow test case, focusing on pressure reconstruction. NOF’s ability to *directly* infer pressure from PIV images through an OF-based approach sets it apart from other techniques. Figure 13 shows a comparison between the exact and reconstructed vorticity and pressure fields. The reconstructed fields demonstrate strong alignment with the ground truth, both qualitatively and quantitatively, capturing key features such as vortical structures, pressure drops within vortex centers, and the absence of vorticity in regions dominated by mean flow. Minor discrepancies appear in regions with steep vorticity gradients, where subtle smoothing is observed in the reconstruction. However, the low NRMSE values (11.3% for vorticity and 16.8% for pressure) affirm the accuracy of our results.

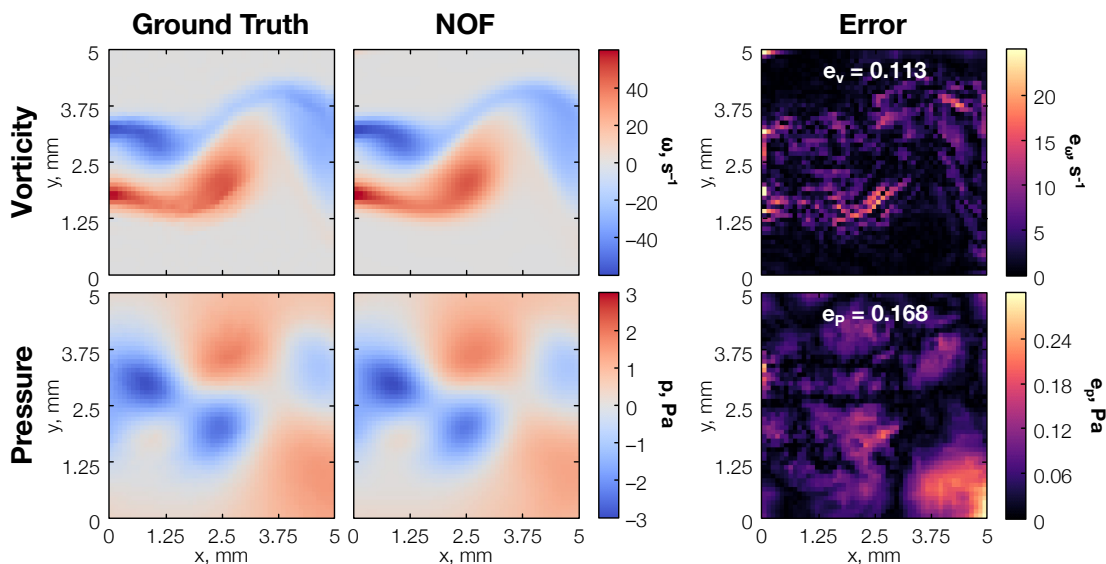


Figure 13: Exact and reconstructed cylinder flow vorticity fields (top) and pressure fields (bottom) with corresponding point-wise error fields (right). NRMSEs are superimposed on the absolute error plot.

While a pressure Poisson solver could estimate the pressure field from the velocity field in this pseudo-2D flow, this approach often amplifies errors, as any inaccuracies in the velocity field propagate into the pressure solution, with no mechanism to correct the velocity field based on pressure. Regularization is typically needed to counteract these issues [70, 71]. Conversely, NOF-phys reconstructs pressure and velocity together, allowing each field to enhance the other through the Navier–Stokes residuals embedded in the penalty term. This coupling minimizes inconsistencies, ensuring that both pressure and velocity reconstructions remain well-aligned with governing physical laws and observed image data.

## 5 Experimental Results

### 5.1 Vortex Flow

Next, we discuss experimental results for a vortex flow in the wake of an airfoil. Figure 14 compares the velocity magnitude and vorticity fields reconstructed by CC, WOF, and NOF. While hyperparameter selection for CC and NOF was straightforward, WOF required extensive tuning due to its sensitivity to noise. For WOF, we tested over 30 hyperparameter combinations before selecting what we deemed to be the best result, which still shows artifacts near the corner of the field. Many other combinations produced larger artifacts closer to the vortex core. Both CC and WOF exhibit grainy textures due to image noise, whereas NOF is more resilient to these effects. The vorticity fields highlight this noise sensitivity, particularly near the vortex core, where both CC and WOF produce artifacts that distort the expected vortex shape.

Figure 15 showcases horizontal cut plots of both velocity components and vorticity, taken slightly offset from the vortex core at  $x_2 = 490$  px. The vorticity plot reveals the impact of noise on the reconstructions: while CC and WOF exhibit a few similar spikes, most of them are inconsistent between the two methods, suggesting they are in fact non-physical artifacts. Additionally, both the  $v_1$  and vorticity cut plots display clear artifacts within the vortex core. The vortex core in these images shows signs of significant tracer

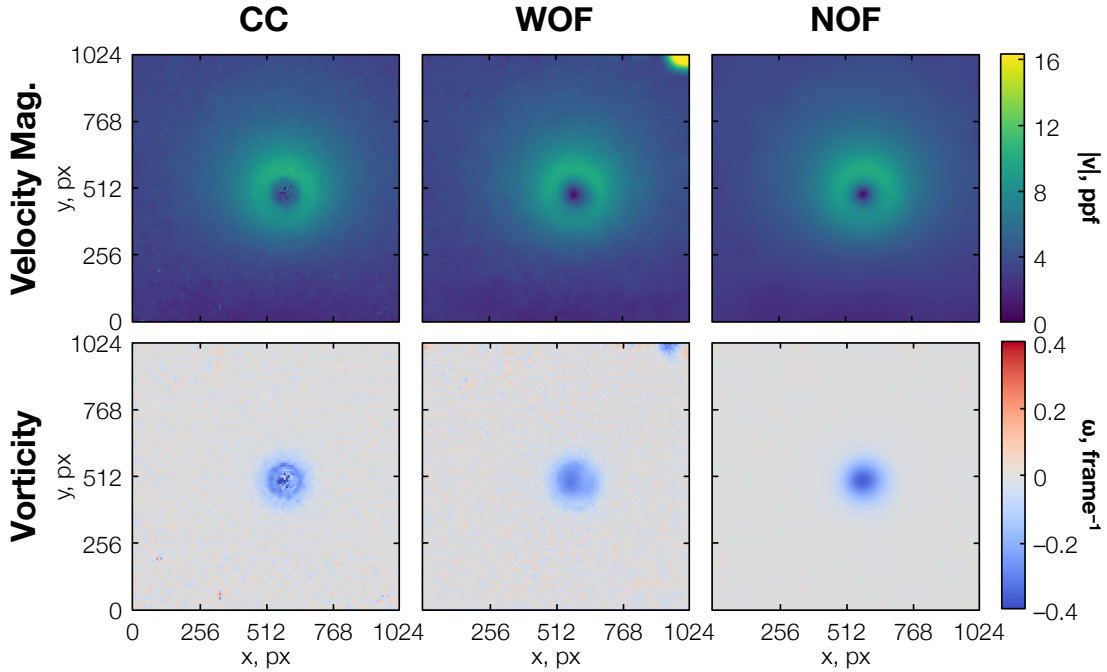


Figure 14: Reconstructed vortex flow velocity magnitude fields (top) and vorticity fields (bottom).

thinning, implying that the particles are subject to inertial transport rather than passively following the surrounding fluid. Tracer thinning complicates the accurate reconstruction of flow in the core region, and the inertial behavior means the reconstructed fields will not perfectly represent the true fluid velocity field.

While it is difficult to conclusively determine if NOF provides a more accurate reconstruction due to the absence of ground truth data, NOF aligns more closely with the expected analytical shape of a vortex than either CC or WOF. These results indicate that NOF may be more resilient to noise than CC or WOF, though further research is needed to quantitatively assess the impact of noise on NOF’s performance.

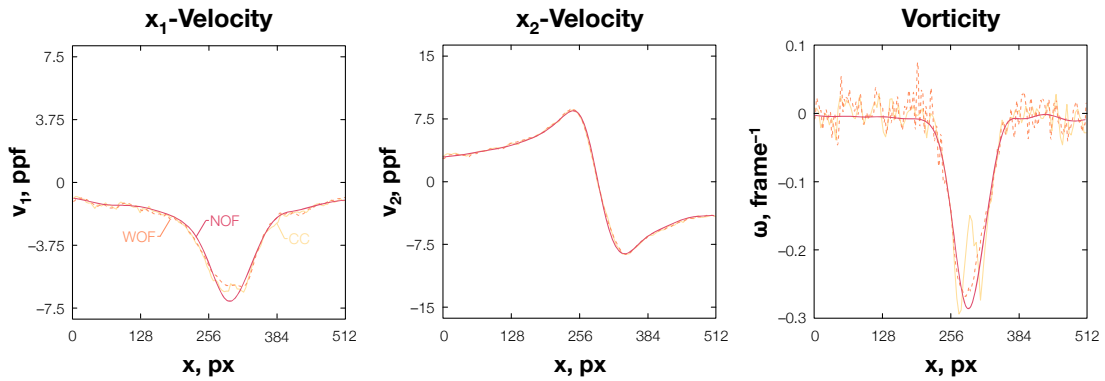


Figure 15: Reconstructed vortex flow  $v_1$  cutplots (left),  $v_2$  cutplots (middle), and vorticity cutplots (right).

## 5.2 Turbulent Jet Flow

We now present the results of the turbulent jet flow case. Unlike the simpler hyperparameter selection in the vortex flow case, the jet flow contains significant energy content across a broad range of frequencies, comparable to the 3D HIT field, requiring a large Fourier encoding to accurately capture its dynamics. However, the increased expressivity needed for this representation also makes NOF more prone to noise-related artifacts. To address this, we applied the div-curl regularization penalty from Eq. (22), which mitigates noise artifacts while preserving the network’s ability to represent the flow accurately.

Figure 16 displays the velocity magnitude and vorticity fields, along with a close-up of the vorticity field within a region of interest, highlighted by the dashed box. To aid visualization, we masked the surrounding

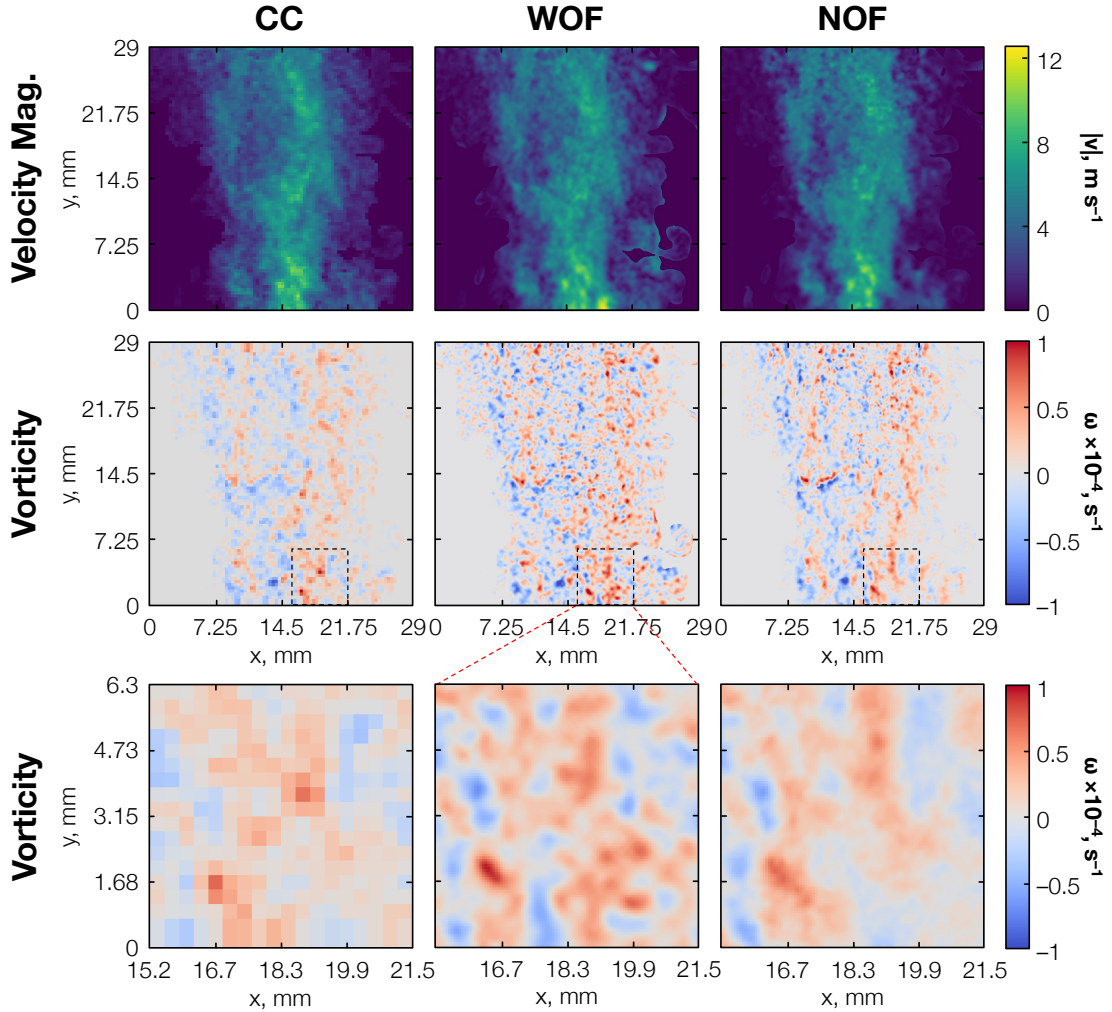


Figure 16: Reconstructed jet flow velocity magnitude fields (top), vorticity fields (middle), and vorticity field inserts (bottom).

flow region outside the jet, where no particles were present (see Fig. 3). These masks were generated by Gaussian blurring the particle images and thresholding them with an empirically determined value.

As shown in Fig. 16, WOF exhibits pronounced “edge effects” where the flow transitions from a tracer-rich region to a tracer-free one. A broader comparison of the vorticity fields reveals that NOF and CC generate more consistent structures, while WOF introduces (what appear to be) spurious fluctuations, similar to those observed in Sec. 4.2. The close-up of the vorticity field highlights an edge effect unique to WOF, absent in both NOF and CC. Given the lack of particle information in this region (see Fig. 3), it is reasonable to speculate that NOF and CC are producing more reliable estimates at the periphery of the jet, while WOF’s artifacts are likely caused by sensitivity to variable seeding density across the image.

While it is challenging to definitively determine which method performs best with experimental data, WOF and NOF likely exhibit similar error patterns, as suggested by the synthetic results in Sec. 4.2, particularly given the comparable turbulence and spectral content of these cases. Further investigation is needed to quantify the impact of noise on NOF performance, especially in comparison to state-of-the-art methods like WOF, to better understand their respective strengths and limitations in experimental settings.

## 6 Conclusions

This manuscript introduces *neural optical flow* (NOF), a neural-implicit method for optical flow (OF) particle image velocimetry (PIV) aimed at improving velocity reconstruction for turbulent flows while providing

a robust framework for data assimilation in PIV. NOF employs a coordinate-based neural network and a differentiable, nonlinear image-warping operator, eliminating the need for a multi-resolution scheme. Its neural-implicit representation simplifies data assimilation and enables direct pressure reconstruction for 2D and pseudo-2D flows. Furthermore, NOF offers an integrated stereo PIV framework that overcomes the limitations of traditional stereo PIV algorithms, which rely on stitching together separate 2D2C velocity estimates.

We evaluated NOF on both synthetic and experimental datasets, comparing its performance to wavelet-based optical flow (WOF) and cross-correlation (CC), two state-of-the-art PIV techniques. In summary, our key findings are:

1. Vanilla NOF provides slightly better velocity reconstructions compared to WOF in planar PIV due to its nonlinear image-warping scheme and inherent suppression spurious high-frequency content.
2. Applying a hard constraint on mass continuity for incompressible 2D/pseudo-2D flows significantly enhances reconstruction quality by constraining NOF to solenoidal solutions, reducing artifacts in high-frequency regions, particularly above the Nyquist frequency.
3. NOF’s all-in-one stereo reconstruction framework eliminates the error-amplifying recombination step required in traditional stereo algorithms. In our tests, this approach limited the increase in error when going from 2D2C to 2D3C estimates to just 0.8%, compared to 4.4% for WOF. Moreover, the out-of-plane energy spectra of NOF are free of spurious high-frequency artifacts, further validating the accuracy of our technique.
4. NOF enables the direct inference of latent fields such as pressure, which is demonstrated in Sec. 4.3. Direct pressure reconstruction improves flow estimation through data assimilation, as quantified in Table 2, offering a robust alternative to post-processing with a pressure Poisson solver.

In summary, NOF offers a versatile and adaptable OF framework for PIV, addressing a broad range of fluid measurement challenges, including stereo PIV and pressure from PIV. While its performance matches or slightly surpasses existing state-of-the-art methods in simpler cases, NOF provides marked advantages beyond these performance gains for complex flows and stereo imaging. Additional benefits include smoother reconstructions in situations with limited, high-frequency data, enhanced feature extraction, and more accurate derivative-based flow statistics, especially in turbulent flows.

## Appendix A The Camera Transform

### Appendix A.1 Forward Transform

Projecting points from world space to image space requires a camera model, with the pinhole camera often providing sufficient accuracy for PIV imaging. For a distortion-free pinhole model, the forward camera transform is defined as

$$\mathbf{s} = \zeta^{-1} \mathbf{K} (\mathbf{R}\mathbf{x} + \mathbf{t}). \quad (34)$$

where  $\mathbf{K}$  is the  $2 \times 3$  intrinsic matrix,  $\mathbf{R}$  is a  $3 \times 3$  orthonormal rotation matrix, and  $\mathbf{t}$  is the translation vector. This vector is defined as  $\mathbf{t} = -\mathbf{R}\mathbf{c}$ , where  $\mathbf{c}$  is the camera’s position in world coordinates. The scale factor  $\zeta$  ensures projection onto the image plane and is defined as

$$\zeta = \mathbf{R}_{3,*} \mathbf{x} + t_3, \quad (35)$$

where  $\mathbf{R}_{3,*}$  is the third row of  $\mathbf{R}$  and  $t_3$  is the third element of  $\mathbf{t}$ .

The intrinsic parameters in  $\mathbf{K}$  include the distance from the pinhole to the sensor,  $\hat{f}$ , which defines the focal length of a pinhole camera, and the principal point,  $\mathbf{s}_0 = (s_{0,1}, s_{0,2})$ , where the optical axis intersects the sensor. Using these elements, the intrinsic matrix is

$$\mathbf{K} = \begin{bmatrix} \psi_1 \hat{f} & 0 & s_{0,1} \\ 0 & \psi_2 \hat{f} & s_{0,2} \end{bmatrix}. \quad (36)$$

The terms  $\psi_1 \hat{f}$  and  $\psi_2 \hat{f}$  represent the effective focal lengths in pixel units along the horizontal and vertical directions; for square pixels,  $\psi_1 = \psi_2 = \psi$ . Note that the focal length of a pinhole camera,  $\hat{f}$ , differs from that of a physical lens,  $f$ . The relationship between these quantities is given by

$$\hat{f} = f \left( 1 + \frac{f}{d_o - f} \right), \quad (37)$$

where  $d_o$  is the distance from the aperture (or pinhole) to the object plane [72].

Lens distortions can be incorporated using a distortion model, typically applied to the normalized image coordinates, i.e., before scaling by the intrinsic matrix,

$$\mathbf{s}' = \zeta^{-1} (\mathbf{R}\mathbf{x} + \mathbf{t}), \quad (38)$$

where  $(\cdot)'$  indicates a normalized quantity and  $\mathbf{s} = \mathbf{K}\mathbf{s}'$ . Radial and tangential distortions are computed using Brown's polynomial distortion model [73, 74],

$$\mathbf{s}'_{\text{dist}} = \mathcal{D}(\mathbf{s}'). \quad (39)$$

This function includes additional intrinsic parameters: specifically, a set of radial and tangential distortion coefficients. Bringing these elements together, the transform for a pinhole camera with distortions is

$$\mathbf{s} = \mathbf{K} \underbrace{\mathcal{D} \left[ \zeta^{-1} (\mathbf{R}\mathbf{x} + \mathbf{t}) \right]}_{\Psi(\mathbf{x})}. \quad (40)$$

In practice, the intrinsic and extrinsic parameters in  $\mathbf{K}$ ,  $\mathbf{R}$ ,  $\mathbf{t}$ , and  $\mathcal{D}$  must be obtained through a camera calibration procedure, while  $\psi$  is a fixed physical property of the sensor.

## Appendix A.2 Inverse Transform

The inverse mapping from sensor coordinates to world coordinates,  $\mathbf{s}$  to  $\mathbf{x}$ , involves inverting the forward projection function in Eq. (40). Each pixel corresponds to a line through world space, and specifying the distance along this line,  $l$ , determines a unique 3D position. In planar and stereo PIV, this is the distance where the line intersects the laser sheet, as discussed in the following sections.

The general inverse transform is

$$\mathbf{x} = \underbrace{\frac{l}{\|\mathbf{r}\|_2} \mathbf{R}^\top \begin{bmatrix} \mathbf{K}^{-1}\mathbf{s} - \mathbf{s}'_0 \\ 1 \end{bmatrix}}_{\Psi^{-1}(\mathbf{s}, l)} + \mathbf{c}, \quad (41)$$

where  $\mathbf{r}$  is a ray-direction vector;  $\mathbf{K}^{-1}$  and  $\mathbf{s}'_0$  are defined as

$$\mathbf{K}^{-1} \equiv \hat{f}^{-1} \begin{bmatrix} \psi_1^{-1} & 0 \\ 0 & \psi_2^{-1} \end{bmatrix} \quad \text{and} \quad \mathbf{s}'_0 \equiv \hat{f}^{-1} \begin{bmatrix} s_{0,1}/\psi_1 \\ s_{0,2}/\psi_2 \end{bmatrix}. \quad (42)$$

When lens distortions are significant, the undistorted sensor coordinates must be found by inverting the distortion model,

$$\mathbf{s}_{\text{dist}} = \mathbf{K} \mathcal{D}(\mathbf{K}^{-1}\mathbf{s} - \mathbf{s}'_0), \quad (43)$$

which is iteratively solved. Here,  $\mathbf{s}_{\text{dist}} = \mathbf{K}\mathbf{s}'_{\text{dist}}$  is a pixel centroid and the solution  $\mathbf{s}$  is used in Eq. (41).

## Appendix A.3 Application to Planar PIV

In planar PIV, the camera is positioned perpendicular to the laser sheet, with the optical axis parallel to the  $x_3$ -axis of the world coordinate system. The world origin is set at the center of the laser sheet, and the camera's position is  $\mathbf{c} = (0, 0, -d_o)$ , where  $d_o$  is the object distance. Since the world and camera coordinate systems are perfectly aligned,  $\mathbf{R}$  is the identity matrix.

Assuming no distortion and that the measurement domain lies within the  $x_1-x_2$  plane (i.e.,  $x_3 = 0$ ), the forward camera transform simplifies to

$$\mathbf{s} = \left( \psi_1 \hat{f} \frac{x_1}{d_o} + s_{0,1}, \psi_2 \hat{f} \frac{x_2}{d_o} + s_{0,2} \right) \quad (44a)$$

and the inverse transform is given by

$$\mathbf{x} = \frac{d_o}{\hat{f}} \left( \frac{s_1 - s_{0,1}}{\psi_1}, \frac{s_2 - s_{0,2}}{\psi_2}, 0 \right). \quad (44b)$$

While minor misalignments and lens distortions are inevitable in a real experiment, they can often be neglected in planar PIV. The full transforms in [Appendix A.1](#) and [Appendix A.2](#) can be used to handle cases with significant alignment and distortion issues.

## Appendix A.4 Application to Stereo PIV

### Appendix A.4.1 Translational Configuration

The translational stereo PIV configuration builds on conventional planar PIV by using two cameras positioned to capture the laser sheet from slightly different perspectives. The object plane, lens plane, and sensor planes of both cameras are all parallel. In a symmetric configuration (see [Fig. 2](#)), the left and right camera positions in world space are

$$\mathbf{c}_L = \left( -\frac{L}{2}, 0, -d_o \right) \quad (45a)$$

and

$$\mathbf{c}_R = \left( \frac{L}{2}, 0, -d_o \right), \quad (45b)$$

where  $L$  is the distance between the camera lenses, and subscripts ‘‘L’’ and ‘‘R’’ indicate the left and right cameras. Assuming perfect alignment with no lens distortion,  $\mathbf{R} = \mathbf{I}$  and the forward camera transforms become

$$\mathbf{s}_L = \left( \psi_1 \hat{f} \frac{x_1 + L/2}{x_3 + d_o} + s_{0,1}, \psi_2 \hat{f} \frac{x_2}{x_3 + d_o} + s_{0,2} \right) \quad (46a)$$

and

$$\mathbf{s}_R = \left( \psi_1 \hat{f} \frac{x_1 - L/2}{x_3 + d_o} + s_{0,1}, \psi_2 \hat{f} \frac{x_2}{x_3 + d_o} + s_{0,2} \right) \quad (46b)$$

These equations are consistent with previous derivations [[2](#), [75](#)]. The inverse transforms, which map image coordinates back to world coordinates, are given by

$$\mathbf{x}_L = \left[ (d_o + x_3) \frac{s_1 - s_{0,1}}{\psi_1 \hat{f}} - \frac{L}{2}, (d_o + x_3) \frac{s_2 - s_{0,2}}{\psi_2 \hat{f}}, x_3 \right] \quad (47a)$$

and

$$\mathbf{x}_R = \left[ (d_o + x_3) \frac{s_1 - s_{0,1}}{\psi_1 \hat{f}} + \frac{L}{2}, (d_o + x_3) \frac{s_2 - s_{0,2}}{\psi_2 \hat{f}}, x_3 \right]. \quad (47b)$$

While particles may be advected out of the measurement plane ( $x_3 \neq 0$ ), stereo PIV assumes that the particles remain within the laser sheet, so we restrict all initial particle positions to the  $x_1$ – $x_2$  plane, with  $x_3 = 0$ . This simplification aligns with the planar assumption commonly used in stereo PIV.

Stereo PIV combines two 2D2C displacement fields, computed from each camera view using a method like CC or OF, into a single 2D3C displacement field in world space. Assuming square pixels,  $\psi_1 = \psi_2 = \psi$ , the relationship between the physical vector,  $\Delta \mathbf{x} = (\Delta x_1, \Delta x_2, \Delta x_3)$ , and the image displacement vectors,  $\Delta \mathbf{s}_L$  and  $\Delta \mathbf{s}_R$ , can be expressed as

$$\Delta x_1 = \frac{\Delta s_{R,1} (x_1 + L/2) - \Delta s_{L,1} (x_1 - L/2)}{\psi M L + (\Delta s_{L,1} - \Delta s_{R,1})} \quad (48a)$$

$$\Delta x_2 = \frac{x_2 \Delta x_3}{d_o} + \frac{\Delta s_{L,2} + \Delta s_{R,2}}{2\psi M} \left( \frac{\Delta x_3}{d_o} + 1 \right) \quad (48b)$$

$$\Delta x_3 = \frac{-d_o (\Delta s_{L,1} - \Delta s_{R,1})}{\psi M L + (\Delta s_{L,1} - \Delta s_{R,1})}. \quad (48c)$$

Since each 3C displacement vector in world space corresponds to two 2C displacement vectors in image space (four pieces of information), the stereo analysis is overdetermined. This redundancy can be leveraged to improve the accuracy of [Eq. \(48b\)](#), e.g., by averaging  $\Delta s_{L,2}$  and  $\Delta s_{R,2}$ , explaining the asymmetry between [Eqs. \(48a\)](#) and [\(48b\)](#).

### Appendix A.4.2 Rotational Configuration

Rotational stereo PIV employs inward-facing cameras, each aimed at the center of the laser sheet. Scheimpflug adapters are commonly used to ensure that the entire sheet remains in focus.<sup>3</sup> When the Scheimpflug condition is met, the object, lens, and sensor planes all intersect along a common line. This contrasts with the standard pinhole model in Eq. (34), which assumes parallel alignment between the lens and sensor planes.

Cornic et al. [78] developed a modified pinhole model to account for the sensor tilt introduced by a Scheimpflug adapter,

$$\mathbf{s} = \zeta^{-1} \mathbf{K} \mathbf{S} \mathbf{R}_\alpha (\mathbf{R} \mathbf{x} + \mathbf{t}), \quad (49)$$

where  $\mathbf{R}_\alpha$  is the rotation matrix accounting for sensor tilt,  $\mathbf{S}$  is the Scheimpflug matrix, and

$$\zeta = (0, 0, 1) \cdot [\mathbf{S} \mathbf{R}_\alpha (\mathbf{R} \mathbf{x} + \mathbf{t})] \quad (50)$$

is the scale factor that projects world coordinates onto the image plane. The sensor rotation matrix  $\mathbf{R}_\alpha$  can be decomposed into rotations about the  $s_1$  and  $s_2$  axes, with respective tilt angles  $\alpha_1$  and  $\alpha_2$ ,

$$\mathbf{R}_\alpha = \begin{bmatrix} \cos(\alpha_2) & 0 & \sin(\alpha_2) \\ 0 & 1 & 0 \\ -\sin(\alpha_2) & 0 & \cos(\alpha_2) \end{bmatrix} \begin{bmatrix} 1 & 0 & 0 \\ 0 & \cos(\alpha_1) & \sin(\alpha_1) \\ 0 & -\sin(\alpha_1) & \cos(\alpha_1) \end{bmatrix}. \quad (51)$$

The Scheimpflug matrix  $\mathbf{S}$  depends on these same tilt angles,

$$\mathbf{S} = \begin{bmatrix} \cos(\alpha_1) \cos(\alpha_2) & 0 & \sin(\alpha_2) \\ 0 & \cos(\alpha_1) \cos(\alpha_2) & -\cos(\alpha_2) \sin(\alpha_1) \\ 0 & 0 & 1 \end{bmatrix}. \quad (52)$$

Lens distortions are modeled similarly to Eq. (39). Incorporating the distortion model, the forward camera transform becomes

$$\mathbf{s} = \mathbf{K} \mathcal{D} \left[ \zeta^{-1} \mathbf{S} \mathbf{R}_\alpha (\mathbf{R} \mathbf{x} + \mathbf{t}) \right]. \quad (53)$$

For the inverse transform, where the goal is to map from sensor coordinates to world coordinates, we assume a laser sheet at the origin with a normal vector  $(0, 0, 1)$ . The resultant inverse mapping is

$$\mathbf{x} = -\frac{c_3}{r_3} \mathbf{r} + \mathbf{c}, \quad (54a)$$

where the ray direction is

$$\mathbf{r} = \mathbf{R}^\top \mathbf{R}_\alpha^\top \mathbf{S}^{-1} \begin{bmatrix} \mathbf{K}^{-1} \mathbf{s} - \mathbf{s}'_0 \\ 1 \end{bmatrix}, \quad (54b)$$

Here,  $c_3$  and  $r_3$  are the third components of  $\mathbf{c}$  and  $\mathbf{r}$ , respectively. As before, if lens distortions are present, the distortion model must be inverted to recover the undistorted sensor coordinates using Eq. (43).

## Appendix B Network Architecture

In this work, we use a coordinate neural network to represent flow fields in  $\mathcal{P}$ . The network consists of an input layer, an output layer, and a series of  $n_1$  hidden layers,

$$\mathbf{z}_{\text{out}} = \overbrace{\mathbf{W}^{n_1+1} \left[ \mathcal{L}^{n_1} \circ \mathcal{L}^{n_1-1} \circ \dots \circ \mathcal{L}^2 \circ \mathcal{F}(\mathbf{z}_{\text{in}}) \right]}^{\mathcal{N}(\mathbf{z}_{\text{in}})} + \mathbf{b}^{n_1+1}, \quad (55a)$$

with

$$\mathbf{z}^l = \underbrace{\sigma(\mathbf{W}^l \mathbf{z}^{l-1} + \mathbf{b}^l)}_{\mathcal{L}^l(\mathbf{z}^{l-1})} \quad \text{for } l \in \{2, 3, \dots, n_1\}. \quad (55b)$$

<sup>3</sup>Rotational configurations can be implemented without Scheimpflug adapters, though the aperture must be stopped down as far as possible to achieve a sufficient depth-of-focus [55, 76, 77].

In this paper,  $\mathbf{z}_{\text{in}}$  is  $(\mathbf{x}, t)$  and  $\mathbf{z}_{\text{out}}$  is  $\mathbf{v}$ .<sup>4</sup> The vector  $\mathbf{z}^l$  contains the values of neurons in the  $l$ th layer,  $\mathbf{W}^l$  and  $\mathbf{b}^l$  are the weight matrix and bias vector, and  $\sigma$  is a nonlinear activation function that is applied element-wise. We apply the weight normalization technique of Salimans and Kingma [79] to accelerate training; we also use GELU activation functions, which showed comparable performance to other non-saturating functions, such as swish, and outperformed hyperbolic tangent functions in preliminary tests.

To mitigate the low-frequency spectral bias inherent in gradient-based optimizers [80], we replace the first hidden layer,  $\mathcal{L}^1$ , with a Fourier encoding layer [81],

$$\mathbf{z}^1 = \underbrace{\left[ \sin(2\pi\boldsymbol{\omega}_1 \cdot \mathbf{z}^0), \cos(2\pi\boldsymbol{\omega}_1 \cdot \mathbf{z}^0), \dots, \sin(2\pi\boldsymbol{\omega}_w \cdot \mathbf{z}^0), \cos(2\pi\boldsymbol{\omega}_w \cdot \mathbf{z}^0) \right]}_{\mathcal{F}(\mathbf{z}_{\text{in}})} \quad (56)$$

Here,  $w$  is the number of Fourier features, and each  $\boldsymbol{\omega}$  is a vector of random frequencies, sampled from a normal distribution and fixed before training. As discussed in Sec. 2.1, the standard deviation of the frequency distribution acts as an implicit regularization mechanism by introducing a controlled spectral bias, which smooths the fields. For time-resolved data, the spatial and temporal standard deviations are adjusted independently to account for variations in spectral content.

The network size (depth and width) is crucial for ensuring its ability to represent the target function. We tested architectures with 7–12 hidden layers and 200–600 neurons per layer, observing consistent results across all configurations. A network with nine hidden layers and 500 neurons per layer provided sufficient representation across all tested flow cases, and therefore was used throughout the study.

The Adam optimizer [82] was employed with a constant learning rate of  $10^{-3}$ . Training durations varied depending on the flow scenario and are reported throughout the paper on a per-case basis. All experiments were implemented using PyTorch 2.4 on an NVIDIA RTX 3090 GPU.

## Appendix C Interpolation Schemes

Approximating the integral in Eq. (8a) requires continuous sampling of the intensity field, which is recorded as a discrete image signal. We tested both bilinear and bicubic interpolation schemes, which provide smooth, differentiable representations of the intensity field. These schemes are essential for our image warping operator to perform accurately during optimization.

Let  $\mathbf{s}_{i,j}$  be the centroid of the  $(i, j)$ th pixel and  $I_{i,j}$  be its intensity. The image vector for an  $m \times n$  image is  $\mathbf{I} = \{I_{i,j} \mid i = 1, \dots, m, j = 1, \dots, n\}$ . Assuming pixels with a side length of one, the bilinear interpolation operator  $\mathcal{B}$  is

$$\hat{\mathbf{I}}(\mathbf{s}) = \overbrace{w_1 I_{i,j} + w_2 I_{i+1,j} + w_3 I_{i,j+1} + w_4 I_{i+1,j+1}}^{\mathcal{B}(\mathbf{I}, \mathbf{s})}, \quad (57a)$$

where the interpolation weights are

$$w_1 = (1 - s_1 + s_{i,j,1}) (1 - s_2 + s_{i,j,2}), \quad (57b)$$

$$w_2 = (s_1 - s_{i,j,1}) (1 - s_2 + s_{i,j,2}), \quad (57c)$$

$$w_3 = (1 - s_1 + s_{i,j,1}) (s_2 - s_{i,j,2}), \quad \text{and} \quad (57d)$$

$$w_4 = (s_1 - s_{i,j,1}) (s_2 - s_{i,j,2}), \quad (57e)$$

where  $\mathbf{s}$  is the query point, enclosed by the centroids  $\mathbf{s}_{i,j}$ ,  $\mathbf{s}_{i+1,j}$ ,  $\mathbf{s}_{i,j+1}$ , and  $\mathbf{s}_{i+1,j+1}$ . This method provides a suitable approximation of intensity across the image.

Bicubic interpolation, on the other hand, uses a 16-pixel neighborhood and computes weights based on polynomial functions of the distances between the query point and pixel centroids. This method captures more detail and provides a higher-order representation than bilinear interpolation, especially near edges of the image. We use the convolution-based implementation from Keys [83], setting the interpolation parameter to  $-0.75$ , as recommended for optimal smoothness. Further technical details on both interpolation schemes can be found in *Numerical Recipes* [84].

<sup>4</sup>The output  $\mathbf{z}_{\text{out}}$  is  $\varphi$  or  $\boldsymbol{\varphi}$  for 2D and 3D velocity fields with a hard constraint on continuity, as discussed in Sec. 2.5, and pressure is outputted when using a Navier–Stokes penalty term,  $\mathbf{z}_{\text{out}} = (\mathbf{v}, p)$  or  $(\varphi, p)$ .

In our implementation, we use the `grid.sample` function in PyTorch for both forms of interpolation. Preliminary tests indicated that bilinear interpolation offers sufficient accuracy at lower computational cost, so it is used as the default throughout this work, unless otherwise stated.

## Acknowledgements

This research was supported by Mitsubishi Electric Research Laboratories (MERL). S.J.G. acknowledges support from Friedrich-Alexander-Universität Erlangen-Nürnberg. J.P.M. acknowledges support from the Department of Defense (DoD) through the National Defense Science and Engineering Graduate (NDSEG) Fellowship Program.

## References

- [1] J. Westerweel, G. E. Elsinga, and R. J. Adrian, "Particle image velocimetry for complex and turbulent flows," *Annu. Rev. Fluid Mech.* **45**, 409–436 (2013).
- [2] M. Raffel, C. E. Willert, F. Scarano, C. J. Kähler, S. T. Wereley, and J. Kompenhans, "Physical and technical background," in "Particle Image Velocimetry: A Practical Guide," (Springer, 2018), pp. 33–111.
- [3] F. Scarano, "Tomographic PIV: principles and practice," *Meas. Sci. Technol.* **24**, 012001 (2012).
- [4] R. J. Adrian, "Twenty years of particle image velocimetry," *Exp. Fluids* **39**, 159–169 (2005).
- [5] J. Westerweel, "Fundamentals of digital particle image velocimetry," *Meas. Sci. Technol.* **8** (1997).
- [6] H. Hu, T. Saga, T. Kobayashi, K. Okamoto, and N. Taniguchi, "Evaluation of the cross correlation method by using PIV standard images," *J. Visualization* **1**, 87–94 (1998).
- [7] C. J. Kähler, S. Scharnowski, and C. Cierpka, "On the resolution limit of digital particle image velocimetry," *Exp. Fluids* **52**, 1629–1639 (2012).
- [8] B. E. Schmidt and J. A. Sutton, "High-resolution velocimetry from tracer particle fields using a wavelet-based optical flow method," *Exp. Fluids* **60** (2019).
- [9] D. P. Hart, "Super-resolution PIV by recursive local-correlation," *J. Visualization* **10**, 1–10 (1999).
- [10] K. Takehara, R. Adrian, G. Etoh, and K. Christensen, "A Kalman tracker for super-resolution PIV," *Exp. Fluids* **29**, S034–S041 (2000).
- [11] F. Scarano, "Iterative image deformation methods in PIV," *Meas. Sci. Technol.* **13**, R1 (2001).
- [12] A. Susset, J. M. Most, and D. Honoré, "A novel architecture for a super-resolution PIV algorithm developed for the improvement of the resolution of large velocity gradient measurements," *Exp. Fluids* **40**, 70–79 (2006).
- [13] D. Schanz, S. Gesemann, and A. Schröder, "Shake-The-Box: Lagrangian particle tracking at high particle image densities," *Exp. Fluids* **57**, 1–27 (2016).
- [14] T. Lui and L. Shen, "Fluid flow and optical flow," *J. Fluid Mech.* **614**, 253–291 (2008).
- [15] D. Heitz, E. Mémin, and C. Schnörr, "Variational fluid flow measurements from image sequences: synopsis and perspectives," *Exp. Fluids* **48**, 369–393 (2009).
- [16] F. Champagnat, A. Plyer, G. Le Besnerais, B. Leclaire, S. Davoust, and Y. Le Sant, "Fast and accurate PIV computation using highly parallel iterative correlation maximization," *Exp. Fluids* **50**, 1169–1182 (2011).
- [17] C. J. Kähler, T. Astarita, P. P. Vlachos, J. Sakakibara, R. Hain, S. Discetti, R. La Foy, and C. Cierpka, "Main results of the 4th International PIV Challenge," *Exp. Fluids* **57**, 1–71 (2016).

- [18] L. Alvarez, C. A. Castaño, M. García, K. Krissian, L. Mazorra, A. Salgado, and J. Sánchez, “A new energy-based method for 3D motion estimation of incompressible PIV flows,” *Comput. Vision Image Understanding* **113**, 802–810 (2009).
- [19] T. Corpetti, D. Heitz, G. Arroyo, E. Mémin, and A. Santa-Cruz, “Fluid experimental flow estimation based on an optical-flow scheme,” *Exp. Fluids* **40**, 80–97 (2006).
- [20] Y. T. Wu, T. Kanade, C. C. Li, and J. Cohn, “Image registration using wavelet-based motion model,” *Int. J. Comput. Vision* **38**, 129–152 (2000).
- [21] P. Dérian, P. Héas, C. Herzet, and E. Mémin, “Wavelets and optical flow motion estimation,” *Numer. Math. Theory Methods Appl.* **6**, 116–137 (2013).
- [22] S. Mallat, *A Wavelet Tour of Signal Processing* (Academic Press, 1999).
- [23] S. Kadri-Harouna, P. Dérian, P. Héas, and E. Mémin, “Divergence-free wavelets and high order regularization,” *Int. J. Comput. Vision* **103**, 80–99 (2013).
- [24] B. E. Schmidt and J. A. Sutton, “Improvements in the accuracy of wavelet-based optical flow velocimetry (wOFV) using an efficient and physically based implementation of velocity regularization,” *Exp. Fluids* **61** (2020).
- [25] G. R. Jassal and B. E. Schmidt, “Accurate near-wall measurements in wall bounded flows with optical flow velocimetry via an explicit no-slip boundary condition,” *Meas. Sci. Technol.* **34**, 125303 (2023).
- [26] A. Nicolas, F. Zentgraf, M. Linne, A. Dreizler, and B. Peterson, “Assessment and application of wavelet-based optical flow velocimetry (wOFV) to wall-bounded turbulent flows,” *Exp. Fluids* **64**, 50 (2023).
- [27] A. Krizhevsky, I. Sutskever, and G. E. Hinton, “ImageNet Classification with Deep Convolutional Neural Networks,” *Adv. Neural Inf. Process. Sys.* **25** (2012).
- [28] I. Goodfellow, J. Pouget-Abadie, M. Mirza, B. Xu, D. Warde-Farley, S. Ozair, A. Courville, and Y. Bengio, “Generative adversarial nets,” *Adv. Neural Inf. Process. Sys.* **27** (2014).
- [29] D. Silver, A. Huang, C. J. Maddison, A. Gue, L. Sifre, G. van den Driessche, J. Schrittwieser, I. Antonoglou, V. Panneershelvam, M. Lanctot, S. Dieleman, D. Grewe, J. Nham, N. Kalchbrenner, I. Sutskever, T. Lillicrap, M. Leach, K. Kavukcuoglu, T. Graepel, and D. Hassabis, “Mastering the game of Go with deep neural networks and tree search,” *Nat.* **529**, 484–489 (2016).
- [30] J. Redmon and A. Farhadi, “YOLO9000: Better, Faster, Stronger,” in “Proceedings of the IEEE Conference on Computer Vision and Pattern Recognition,” (2017), pp. 7263–7271.
- [31] C. Lagemann, K. Lagemann, W. Schröder, and M. Klaas, “Deep artificial neural network architectures in PIV applications,” in “13th International Symposium on Particle Image Velocimetry,” (2019).
- [32] J. Rabault, J. Kolaas, and A. Jensen, “Performing particle image velocimetry using artificial neural networks: a proof-of-concept,” *Meas. Sci. Technol.* **28**, 125301 (2017).
- [33] Y. Lee, H. Yang, and Z. Yin, “PIV-DCNN: cascaded deep convolutional neural networks for particle image velocimetry,” *Exp. Fluids* **58**, 1–10 (2017).
- [34] S. Cai, S. Zhou, C. Xu, and Q. Gao, “Dense motion estimation of particle images via a convolutional neural network,” *Exp. Fluids* **60**, 1–16 (2019).
- [35] S. Cai, J. Liang, S. Zhou, Q. Gao, C. Xu, R. Wei, S. Wereley, and J. S. Kwon, “Deep-PIV: A new framework of PIV using deep learning techniques,” in “Proceedings of the 13th International Symposium on Particle Image Velocimetry (ISPIV),” (2019).

- [36] M. Oechsle, S. Peng, and A. Geiger, "Unisurf: Unifying neural implicit surfaces and radiance fields for multi-view reconstruction," in "Proceedings of the IEEE/CVF International Conference on Computer Vision," (2021), pp. 5589–5599.
- [37] A. Pumarola, E. Corona, G. Pons-Moll, and F. Moreno-Noguer, "D-nerf: Neural radiance fields for dynamic scenes," in "Proceedings of the IEEE/CVF Conference on Computer Vision and Pattern Recognition," (2021), pp. 10318–10327.
- [38] B. Mildenhall, P. P. Srinivasan, M. Tancik, J. T. Barron, R. Ramamoorthi, and R. Ng, "NeRF: Representing Scenes as Neural Radiance Fields for View Synthesis," *Commun. ACM* **65**, 99–106 (2021).
- [39] M. Tancik, V. Casser, X. Yan, S. Pradhan, B. Mildenhall, P. P. Srinivasan, J. T. Barron, and H. Kretschmar, "Block-nerf: Scalable large scene neural view synthesis," in "Proceedings of the IEEE/CVF Conference on Computer Vision and Pattern Recognition," (2022), pp. 8248–8258.
- [40] M. Raissi, P. Perdikaris, and G. E. Karniadakis, "Physics-informed neural networks: A deep learning framework for solving forward and inverse problems involving nonlinear partial differential equations," *J. Comput. Phys.* **378**, 686–707 (2019).
- [41] M. Raissi, A. Yazdani, and G. E. Karniadakis, "Hidden fluid mechanics: Learning velocity and pressure fields from flow visualizations," *Sci.* **367**, 1026–1030 (2020).
- [42] G. Zang, R. Idoughi, R. Li, P. Wonka, and W. Heidrich, "Intratomo: self-supervised learning-based tomography via sinogram synthesis and prediction," in "Proceedings of the IEEE/CVF International Conference on Computer Vision," (2021), pp. 1960–1970.
- [43] D. Rückert, Y. Wang, R. Li, R. Idoughi, and W. Heidrich, "Neat: Neural adaptive tomography," *ACM Transactions on Graphics (TOG)* **41**, 1–13 (2022).
- [44] D. Kelly and B. Thurow, "Investigation of a neural implicit representation tomography method for flow diagnostics," *Meas. Sci. Technol.* **35**, 056007 (2024).
- [45] Q. He, D. Barajas-Solano, G. Tartakovsky, and A. M. Tartakovsky, "Physics-informed neural networks for multiphysics data assimilation with application to subsurface transport," *Adv. Water Resour.* **141**, 103610 (2020).
- [46] Y. Patel, V. Mons, O. Marquet, and G. Rigas, "Turbulence model augmented physics-informed neural networks for mean-flow reconstruction," *Phys. Rev. Fluids* **9**, 034605 (2024).
- [47] S. Liu, H. Wang, J. H. Chen, K. Luo, and J. Fan, "High-resolution reconstruction of turbulent flames from sparse data with physics-informed neural networks," *Combust. Flame.* **260**, 113275 (2024).
- [48] M. Qi, R. Idoughi, and W. Heidrich, "HDNet: Physics-Inspired Neural Network for Flow Estimation based on Helmholtz Decomposition," (2024).
- [49] S. Cai, H. Li, F. Zheng, F. Kong, M. Dao, G. E. Karniadakis, and S. Suresh, "Artificial intelligence velocimetry and microaneurysm-on-a-chip for three-dimensional analysis of blood flow in physiology and disease," *Proc. Natl. Acad. Sci.* **118** (2021).
- [50] L. P. N. Mendes, A. M. C. Ricardo, A. J. M. Bernardino, and R. M. L. Ferreira, "A comparative study of optical flow methods for fluid mechanics," *Exp. Fluids* **63**, 7 (2022).
- [51] J. P. Molnar, E. J. LaLonde, C. S. Combs, O. Léon, D. Donjat, and S. J. Grauer, "Forward and inverse modeling of depth-of-field effects in background-oriented schlieren," *AIAA J.* pp. 1–14 (2024).
- [52] S. Ullman, "The Interpretation of Visual Motion," (1979).
- [53] B. K. P. Horn and B. G. Schunck, "Determining optical flow," *Artif. Intell.* **17**, 185–203 (1981).
- [54] T. Corpetti, É. Mémin, and P. Pérez, "Dense estimation of fluid flows," *IEEE Trans. Pattern Anal. Mach. Intell.* **24**, 365–380 (2002).

- [55] A. K. Prasad and R. J. Adrian, “Stereoscopic particle image velocimetry applied to liquid flows,” *Exp. Fluids* **15**, 49–60 (1993).
- [56] A. K. Prasad, “Stereoscopic particle image velocimetry,” *Exp. Fluids* **29**, 103–116 (2000).
- [57] J. Kaipio and E. Somersalo, *Statistical and Computational Inverse Problems* (Springer Science & Business Media, 2006).
- [58] J. Yuan, C. Schnörr, and E. Mémin, “Discrete orthogonal decomposition and variational fluid flow estimation,” *J. Math. Imaging Vision* **28**, 67–80 (2007).
- [59] G. Jin, J. C. Wong, A. Gupta, S. Li, and Y. S. Ong, “Fourier warm start for physics-informed neural networks,” *Eng. Appl. Artif. Intell.* **132**, 107887 (2024).
- [60] M. Stark, “Optical Flow PIV: Improving the Accuracy and Applicability of Particle Image Velocimetry,” Master’s thesis, Eidgenössische Technische Hochschule Zürich (2013).
- [61] Y. Chong, J. Liang, T. Chen, C. Xu, and C. Pan, “Unsupervised learning on particle image velocimetry with embedded cross-correlation and divergence-free constraint,” *IET Cyber-Syst. Robot.* **4**, 200–211 (2022).
- [62] K. Zhou, J. Li, J. Hong, and S. J. Grauer, “Stochastic particle advection velocimetry (SPAV): theory, simulations, and proof-of-concept experiments,” *Meas. Sci. Technol.* **34**, 065302 (2023).
- [63] K. Zhou, S. J. Grauer, D. Schanz, P. Godbersen, A. Schröder, T. Rockstroh, Y. J. Jeon, and B. Wieneke, “Benchmarking data assimilation algorithms for 3D Lagrangian particle tracking,” in “21st International Symposium on Applications of Laser and Imaging Techniques to Fluid Mechanics,” (2024), p. 229.
- [64] M. Stanislas, K. Okamoto, and C. Kähler, “Main results of the first International PIV Challenge,” *Meas. Sci. Technol.* **14**, R63 (2003).
- [65] M. Stanislas, K. Okamoto, C. J. Kähler, J. Westerweel, and F. Scarano, “Main results of the third International PIV Challenge,” *Exp. Fluids* **45**, 27–71 (2008).
- [66] J. Carlier and B. Wieneke, “Report 1 on production and diffusion of fluid mechanics images and data,” Tech. rep., FLUID Image analysis and Description (FLUID), 6th EU Research Framework Programme, European Commission (2005).
- [67] E. Perlman, R. Burns, Y. Li, and C. Meneveau, “Data exploration of turbulence simulations using a database cluster,” in “Proceedings of the 2007 ACM/IEEE Conference on Supercomputing,” (2007), pp. 1–11.
- [68] A. J. Jerri, “The Shannon sampling theorem—Its various extensions and applications: A tutorial review,” *Proc. IEEE* **65**, 1565–1596 (1977).
- [69] R. M. Schmidt, F. Schneider, and P. Hennig, “Descending through a Crowded Valley — Benchmarking Deep Learning Optimizers,” in “International Conference on Machine Learning,” (PMLR, 2021), pp. 9367–9376.
- [70] Z. Pan, J. Whitehead, S. Thomson, and T. Truscott, “Error propagation dynamics of PIV-based pressure field calculations: how well does the pressure Poisson solver perform inherently?” *Meas. Sci. Technol.* **27**, 084012 (2016).
- [71] C. Pryce, L. Li, J. P. Whitehead, and Z. Pan, “A simple boundary condition regularization strategy for image velocimetry-based pressure field reconstruction,” *Exp. Fluids* **65**, 1–6 (2024).
- [72] B. Wieneke, “Stereo-PIV using self-calibration on particle images,” *Exp. Fluids* **39**, 267–280 (2005).
- [73] D. Brown, “Decentering distortion of lenses,” *Photogramm. Eng* **32**, 444–462 (1996).

- [74] C. B. Duane, "Close-range camera calibration," *Photogramm. Eng* **37**, 855–866 (1971).
- [75] M. P. Arroyo and C. A. Greated, "Stereoscopic particle image velocimetry," *Meas. Sci. Technol.* **2**, 1181 (1991).
- [76] J. Westerweel and F. T. M. Nieuwstadt, "Performance tests on 3-dimensional velocity measurements with a two-camera digital particle-image velocimeter," in "Laser Anemometry: Advances and Applications," , vol. 1 (American Society of Mechanical Engineers, 1991), pp. 349–355.
- [77] N. J. Lawson and J. Wu, "Three-dimensional particle image velocimetry: error analysis of stereoscopic techniques," *Meas. Sci. Technol.* **8**, 894 (1997).
- [78] P. Cornic, C. Illoul, A. Cheminet, G. Le Besnerais, F. Champagnat, Y. Le Sant, and B. Leclaire, "Another look at volume self-calibration: calibration and self-calibration within a pinhole model of Scheimpflug cameras," *Meas. Sci. Technol.* **27**, 094004 (2016).
- [79] T. Salimans and D. P. Kingma, "Weight normalization: A simple reparameterization to accelerate training of deep neural networks," *Adv. Neural Inf. Process. Syst.* **29** (2016).
- [80] S. Wang, Y. Teng, and P. Perdikaris, "Understanding and mitigating gradient flow pathologies in physics-informed neural networks," *SIAM J. Sci. Comput.* **43**, A3055–A3081 (2021).
- [81] M. Tancik, P. Srinivasan, B. Mildenhall, S. Fridovich-Keil, N. Raghavan, U. Singhal, R. Ramamoorthi, J. Barron, and R. Ng, "Fourier features let networks learn high frequency functions in low dimensional domains," *Adv. Neural Inf. Process. Syst.* **33**, 7537–7547 (2020).
- [82] Z. Zhang, "Improved Adam Optimizer for Deep Neural Networks," in "2018 IEEE/ACM 26th International Symposium on Quality of Service (IWQoS)," (IEEE, 2018), pp. 1–2.
- [83] R. Keys, "Cubic convolution interpolation for digital image processing," *IEEE Trans. Acoust. Speech Signal Process.* **29**, 1153–1160 (1981).
- [84] W. H. Press, *Numerical Recipes 3rd Edition: the Art of Scientific Computing* (Cambridge University Press, 2007).